

Mobile monitoring of urban air quality at high spatial resolution by low-cost sensors: Impacts of COVID-19 pandemic lockdown

Shibao Wang¹, Yun Ma¹, Zhongrui Wang¹, Lei Wang¹, Xuguang Chi¹, Aijun Ding¹, Mingzhi Yao², Yunpeng Li², Qilin Li², Mengxian Wu³, Ling Zhang³, Yongle Xiao³, Yanxu Zhang¹

5 ¹School of Atmospheric Sciences, Nanjing University, Nanjing, China

²Beijing SPC Environment Protection Tech Company Ltd., Beijing, China

³Hebei Saihero Environmental Protection Hi-tech. Company Ltd., Shijiazhuang, China

Correspondence to: Yanxu Zhang (zhangyx@nju.edu.cn)

Abstract. The development of low-cost sensors and novel calibration algorithms provides new hints to complement conventional ground-based observation sites to evaluate the spatial and temporal distribution of pollutants on hyperlocal scales (tens of meters). Here we use sensors deployed on a taxi fleet to explore the air quality in the road network of Nanjing over the course of a year (Oct. 2019 – Sep. 2020). Based on GIS technology, we develop a grid analysis method to obtain 50 m resolution maps of major air pollutants (CO, NO₂, and O₃). Through hotspots identification analysis, we find three main sources of air pollutants including traffic, industrial emissions, and cooking fumes. We find that CO and NO₂ concentrations show a pattern: highways > arterial roads > secondary roads > branch roads > residential streets, reflecting traffic volume. While the O₃ concentrations in these five road types are in opposite order due to the titration effect of NOx. Combined the mobile measurements and the stationary stations data, we diagnose that the contribution of traffic-related emissions to CO and NO₂ are 42.6% and 26.3%, respectively. Compared to the pre-COVID period, the concentrations of CO and NO₂ during COVID-lockdown period decreased for 44.9% and 47.1%, respectively, and the contribution of traffic-related emissions to them both decreased by more than 50%. With the end of the COVID-lockdown period, traffic emissions and air pollutant concentrations rebounded substantially, indicating that traffic emissions have a crucial impact on the variation of air pollutants levels in urban regions. This research demonstrates the sense power of mobile monitoring for urban air pollution, which provides detailed information for source attribution, accurate traceability, and potential mitigation strategies at urban micro-scale.

25 1 Introduction

Urban air pollution poses a serious health threat with >80% of the world's urban residents exposed to air pollution levels that exceed the World Health Organization (WHO) guidelines (WHO, 2016). The global urban air pollution ([measured by PM₁₀ or PM_{2.5}](#)) also deteriorated by 8% during recent years despite improvements in some regions (WHO, 2016). Extremely large spatial variability exists for urban air pollutants [e.g., carbon monoxide (CO), nitrogen dioxide (NO₂), and ozone (O₃)] over scales from kilometer to meters, as a result of complex flow pattern, non-linear chemical reactions, and unevenly distributed emissions from vehicle and industrial activities (Apte et al., 2017; Miller et al., 2020). Here we illustrate an approach to obtain a high-resolution urban air quality map using low-cost sensors deployed on a routinely operating taxi fleet.

High spatio-temporal resolution air quality data is critical to urban air quality management, exposure assessment, epidemiology study, and environmental equity (Apte et al., 2011, 2017; Boogaard et al., 2010). Numerous methodologies have been developed to obtain urban air pollutant concentrations, including stationary monitoring networks (Cavellin et al., 2016), near-roadway sampling (Karner et al., 2010; Zhu et al., 2009; Padro-Martinez et al., 2012), satellite remote sensing (Laughner et al., 2018; Xu et al., 2019), land use regression (LUR) model (Weissert et al., 2020), and chemical transport models (CTMs) (Li et al., 2010). However, the stationary monitoring stations (including near-roadway sampling) are sparse and uneven, and the ability to reflect the details of urban air pollution is limited, especially at remote communities (Snyder et al., 2013). Remote

40 sensing and CTMs are generally spatially coarse (~km resolution), and cannot resolve species that are inert to radiative transfer (e.g. mercury and lead) or without known emission inventory and/or chemical mechanisms. LUR model can estimate concentrations at high spatial resolution, but it provides limited temporal information, and the predicting power is poor in areas with specific local sources (Kerckhoffs et al., 2016).

45 Mobile monitoring is a promising approach to garner high spatial resolution observations representative of the community scale (Miller et al., 2020; Hasenfratz et al., 2015). Different vehicle platforms are used for mobile monitoring, including minivan (Isakov et al., 2007), cargo tricycle (Airparif, 2009), bicycle (Bart et al., 2012), taxi (Le and Cha, 2018), Street View cars (Apte et al., 2017), and city bus (Kaivonen and Ngai, 2020). However, the scale of deployment and subsequent data coverage are limited by the cost of the observation instrument (Bossche et al., 2015). This issue has been addressed by the development of low-cost sensors that are calibrated with machine learning based algorithms (Miskell et al., 50 2018; Shiva et al., 2019; Lim et al., 2019). The emergence of low-cost air monitoring technologies was recognized by the U.S. EPA (Snyder et al., 2013) and European Commission (Kaur et al., 2007), and was also recommended to be incorporated in the next Air Quality Directive (Borrego et al., 2015). For example, Weissert et al. (2020) combined land use information with low-cost sensors to obtain hourly O_3 and NO_2 concentration distributions at a resolution of 50 m. High agreements are also found between well-calibrated low-cost sensor systems and standard instrumentations (Chatzidiakou et al., 2019; Hagan et al., 55 2019).

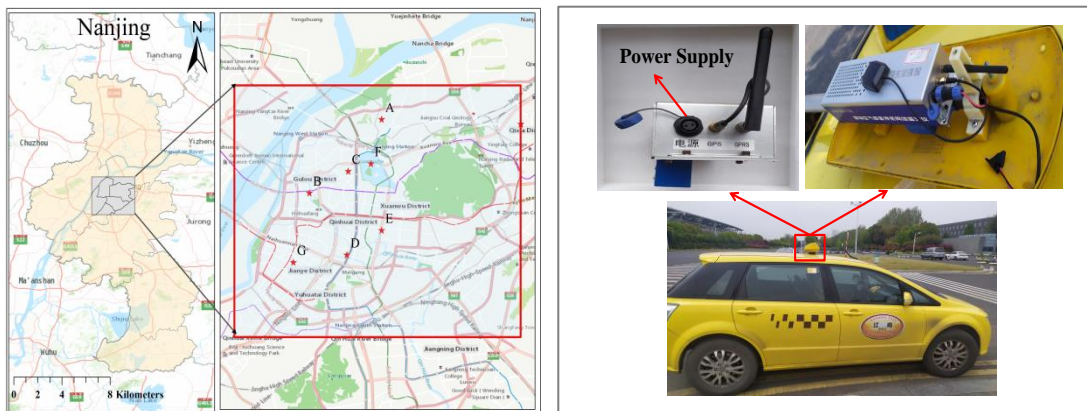
60 The objective of this study is to illustrate the sensing power of low-cost sensors deployed on a routinely operating taxi fleet platform in a megacity. We combine mobile observations and geographic information system (GIS) to obtain the hourly distribution of multiple air pollutants at 50 m resolution. By comparing to the measurements by background sites, the contribution of traffic emission to urban air pollution is also diagnosed. We explore the influencing factors of pollutant levels including time of the day/week and holidays. Moreover, our sampling period covered the outbreak of COVID-19 in China. The pandemic lockdown had a tremendous impact on the socio-economic activities especially the traffic sector, and subsequently the air quality (Zhang et al., 2020; Huang et al., 2020). We evaluate how urban air quality changes at different periods of the pandemic and explore the impact of traffic-related emissions.

2 Material and methods

65 2.1 Mobile monitoring

We use the mobile sampler XHAQSN-508 from Hebei Sailhero Environmental Protection High-tech Co., Ltd. (Hebei, China) to measure the air quality in Nanjing urban area. The instrument is equipped with internal gas sensors for CO, NO_2 , and O_3 (dimensions: 290×81×55 mm; weight: 1.0 kg) as well as two small in-built sensors for temperature and relative humidity, and is fixed in the top lamp support pole (~1.5 m above ground) of two Nanjing taxis (Figure 1). All three sensors are 70 electrochemical-based sensors that can detect gaseous pollutants at levels as low as ppb (Maag et al., 2018). It is continuously powered by an external DC 12V power supply provided by a taxi battery. The sample is refreshed by pumping air to the sensors. There is an air inlet at the bottom of the instrument, which is also checked periodically to avoid blockage. Because it is fixed in the taxi top lamp, it can reduce the impact of different wind direction airflow. This device integrates components for data integration, processing, and transmission, and provides data management, quality control, and visualization functions. 75 The monitoring data is automatically uploaded to a database in the cloud via the 4G telecommunications network. The monitoring system of CO, NO_2 , and O_3 are configured to continuous measure at a frequency of once per 10 seconds, and their limit of detection (LOD) are 0.01 $\mu\text{mol/mol}$, 0.1 nmol/mol , and 0.1 nmol/mol , respectively. Taxis fueled with electricity and liquefied natural gas are selected to reduce the impact of emissions from the sampling vehicles themselves. We continuously measured the concentration of CO, NO_2 , and O_3 in the street canyon in the urban area of Nanjing (with the center located at

80 32.07 °N and 118.72 °E) for a whole year (Oct 1, 2019 - Sep 30, 2020). The sampling routes were relatively random during taxi operations, mainly on the arterial roads. Generally, the sampling campaign is conducted on both weekdays and weekends from 6:00 A.M. to 10:00 P.M. Occasionally the taxi drivers work for the night shift, and the instruments are run from 10:00 P.M. to 6:00 A.M. The collected data covers 373 km² with a population of 6 million (Figure 1).



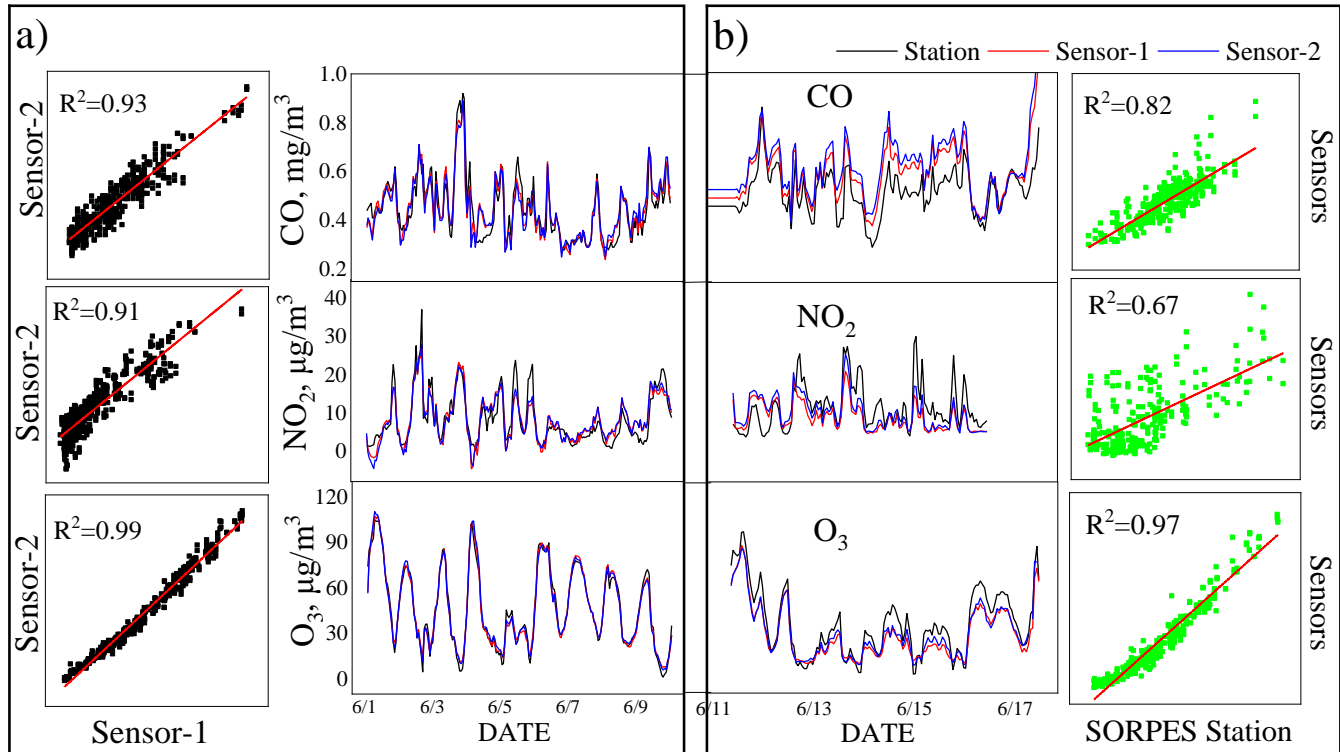
85 **Figure 1.** Location of the monitoring areas in the city of Nanjing (left) and photo of instrument installment (right). Red stars are the locations of stationary stations belonging to the national air quality measurement network of China. These stations cover different functional regions of the city: A, B, C, D, E, F, and G represent industrial, cultural and educational, commercial, traffic, residential, ecological park and new urban area, respectively. Map credit: ESRI 2020.

2.2 Sensors calibration and validation

90 Different from traditional instruments, low-cost sensors have some limitations, such as dynamic boundaries, nonlinear response, signal drift, environmental dependencies, and low selectivity, so it is important that calibration procedures are applied with respect to these limitations (Maag et al, 2018). The sensors are usually trained with co-located data collected by reference methods before being deployed to actual measuring campaigns (Kaivonen and Ngai, 2020; Chatzidiakou et al., 2019; Bossche et al., 2015). The XHAQSN-508 is calibrated every month starting from September, 2019. The instrument is placed at the Station for Observing Regional Processes of the EarthSystem (SORPES) in the Xianlin Campus of Nanjing University (https://as.nju.edu.cn/as_en/obspplatform/list.htm) for at least seven days before the taxi began sampling. The collected data is calibrated against standard instruments (Thermo Fisher Scientific 48i, 42i, and 49i, USA for CO, NO₂, and O₃, respectively) (Ding et al., 2013). Comparing different calibration models, we found that machine learning algorithm can improve sensor/monitor agreement with reference monitors, and many previous studies have used this method (Qin et al., 2020; Esposito et al., 2018; Vito et al., 2018). A supervised machine learning methodology based on the Gradient Boost Decision Tree (GBDT) is used for data calibration (Johnson et al., 2018). GBRT, an ensemble learning method, is a decision tree-based regression model that implements boosting to improve model performance using both parameter selection and k-fold cross validation. GBRT needs to be trained by the dataset with target labels (Yang et al., 2017). It takes input variables including raw signals of sensors, other air pollutants concentrations, temperature and humidity. The stationary instrument data are taken as training targets. The parameters of the machine learning model are adjusted continuously based on gradient descent algorithm. The R² of the calibration results are generally high (> 0.90) for all the three air pollutants (e.g. Figure 2a).

105 The success of supervised model training with target labels (i.e. co-located with SORPES, Figure 2a) does not guarantee for its predicting power for conditions without labels (i.e. on road or co-located with SORPES but not feeding the station data to the algorithm, Figure 2b). We use a calibration-validation methodology to evaluate the performance of the calibrated sensors (Chatzidiakou et al., 2019). This method includes two phases: first, the sampler was calibrated against the SORPES station for 10 days (Jun. 1-10, 2020), and the sensor data were used for sensor algorithm training as above described (Figure 2a); second, we continued to place the sampler in the station (Jun. 11-17, 2020). However, the sensor data are not used for calibration but directly fed in the algorithm trained in the first phase. The results are compared with the station data (i.e. validation phase, Figure 2b). We find that the sensor data agree well with standard instrumentation in the second phase. The sensor retrieved CO,

115 NO₂, and O₃ concentrations are 0.58±0.12 mg/m³, 8.40±4.30 µg/m³, 27.3±16.5 µg/m³ respectively, not significantly different from that by standard instruments (0.50±0.10 mg/m³ and 10.5±6.31 µg/m³, and 32.4±20.2 µg/m³) ($\alpha = 0.05$, ANOVA analysis). The R^2 values remain generally high (0.82-0.97) for different air pollutants (CO and O₃) except NO₂ ($R^2 = 0.67$). The lower R^2 value for NO₂ may be associated with the higher humidity during the validation period (Jun. 13-16, 2020). As NO₂ is water dissolvable, high humidity may lead to a low bias for sensors (Wei et al., 2018). To improve performance of the NO₂ model, 120 temperature and humidity are also involved in the training algorithm. Field calibration of low-cost sensors is still a challenging task, as it is greatly affected by atmospheric composition and meteorological conditions (Spinelle et al., 2017; Castell et al. 2017). Our results have high R^2 values compared to previous studies, indicating relatively high accuracy (e.g. Castell et al. 2017). The results from the two sensors also agree with each other reasonably well, with R^2 values ranged 0.97-0.99 for a linear regression. Their data are thus combined in the following analysis to achieve a maximum data coverage.

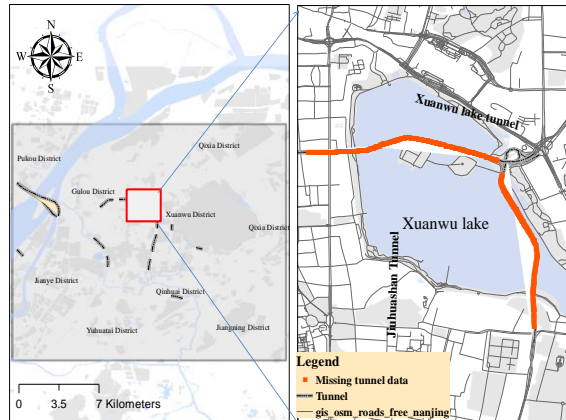


125 **Figure 2.** Sensor performance evaluated by a calibration-validation methodology for CO, NO₂, and O₃. a) calibration period (Jun 1-10, 2020); b) validation period (Jun 11-17, 2020). The time series plots compare the concentrations measured by the co-located sensors and standard instruments, while the scatterplots show linear regressions between them.

2.3 Data processing

130 As the mobile monitoring platform samples along the trajectories of carrying vehicles, we need to either sacrifice the temporal information to calculate the spatial distribution of air pollutants, or the spatial information to temporal variations. Similar approaches have also been adopted by previous studies (Bossche et al., 2015; Apte et al., 2017; Farrell et al. 2015). To generate the spatial distribution of air pollutants at high spatial resolution, we divide the research area into grids with 50 m × 50 m resolution, and calculate the mean values of the samples collected in each grid. The driving condition is highly variable and 135 the taxi can travel more than 50 m in 10 seconds if the vehicle speed is over 18 km/hr. However, given the complexity of the driving conditions, we ignore the vehicle trajectory in the past 10 seconds but assign the measured values to the location of the vehicle at the time of data uploading. Then, combined with GIS technology, we calculate the average of all the data points over one year that fall in the same grid. One drawback of our study is the impact of spike concentrations on sensor performance. The 140 sensors keep reporting high concentrations in an approximate one-minute period after exposure to large environmental concentration spikes. This effect would reduce the effective resolution of our gridded concentration map. Similarly, we average all the samples collected in different grids but in the same hour of the day to get hourly mean concentrations of the

145 sampling domain. The GPS signal is missing when the taxis pass through the nine underground tunnels in Nanjing (e.g. Xuanwu lake tunnel and Jiuahuashan tunnel in the city center, Figure 3). We assume the taxes travel in a constant speed and the sampling points are uniformly allocated along the tunnel. We use the Arcgis 10.2 software for data processing. To calculate the air pollutants concentrations (CO, NO₂, and O₃) map of different road types and the contribution of traffic emissions to them, we divide the urban roads in Nanjing area into five types, including highways, arterial roads, secondary roads, branch roads, and residential streets (<https://wiki.openstreetmap.org/wiki/Key:highway>). Roads and land use data of Nanjing shown in Figure 3 are based on OpenStreetMap (OpenStreetMap contributors, 2020).



150 **Figure 3.** Locations of tunnels in Nanjing urban area. © OpenStreetMap contributors 2019. Distributed under a Creative Commons BY-SA License.

2.4 Traffic source attribution

155 The mobile platform keeps sampling in the urban road network which carries a strong signal from traffic sources. By contrast, stationary stations are often located far away from major roads to represent a regional background air pollution level (Hilker et al., 2019). Seven state-operated air quality observation stations in Nanjing are selected in our research, including Maigaoqiao, Caochangmen, Shanxi Road, Zhonghuamen, Ruijin Road, Xuanwu Lake, and Olympic Sports Center (Zhao et al., 2015; Zou et al., 2017), which are far away from major roads and large point sources, so they are usually used as regional 160 backgrounds in different functional areas (Zou et al., 2017; An et al., 2015). For example, Zou et al. (2017) chose the Olympic Center station (G, Figure 1) to get the background characteristics of CO and NO₂ in Nanjing. Therefore, the contribution from traffic-related emissions can be obtained by differencing the mobile measurements and the stationary ones, following Bossche et al. (2015):

$$AP_{traffic,ij} = (AP_{ij} - AP_{min})/AP_{ij} \quad (1)$$

165 where, $AP_{traffic,ij}$ represents the air pollutant concentration contributed by traffic emissions for the i^{th} pollutant at time j , %; AP_{ij} is the sensor measured air pollutant concentration; and AP_{min} means the ambient background concentration, which is calculated as the minimum of the measurements from all the stations in Nanjing in the national air quality network without major sources within a direct vicinity of 50 m (<https://quotsoft.net/air/>, Figure 1). We refer to this method as “background site (BS)”.

170 We also adopt a method similar to Apte et al. (2017) for traffic source attribution. This method includes a peak detection algorithm to calculate the contribution of local traffic emission sources to on-road pollutant concentrations. We calculate the mean and minimum of air pollutant concentrations in each grid as the “peak” and “baseline”, respectively. The difference between the two is considered as the contribution from traffic sources. We refer to this method as “peak detection (PD)”. Matlab 2019b is used for such data calculation.

3 Results and discussion

3.1 Effect of spatial resolution on reproducibility

There is a trade-off between the resolution of air pollutant concentration map and its reproducibility, i.e. high-resolution maps subject to large randomness due to the limited number of samples in each grid. We investigate the consistency of spatial patterns of different resolution (10-100 m). We calculate the standard error of the means of samples in each grid (SEM), and then averaged the SEM over all grid cells:

$$SEM = \overline{\sigma/\sqrt{n}} \quad (2)$$

where, σ and n are the standard deviation and number of samples in each grid, respectively. We find the calculated SEM first decays rapidly with the grid spacing but tends to be in a regime of linear decay after a resolution of approximately 50 m for all the three air pollutants (Figure 4). Therefore, we choose a resolution of 50 m, which is consistent with previous studies (Bossche et al. 2015; Apte et al. 2017). For example, Bossche et al. (2015) used a spatial resolution of 20-50 m to map urban air quality and identify hotspots. Apte et al. (2017) found that reproducible results (with high precision and low bias) of NO, NO₂, and black carbon can be generated by at least 10-25 repetitions in a specific area with 30 m median spatial aggregation.

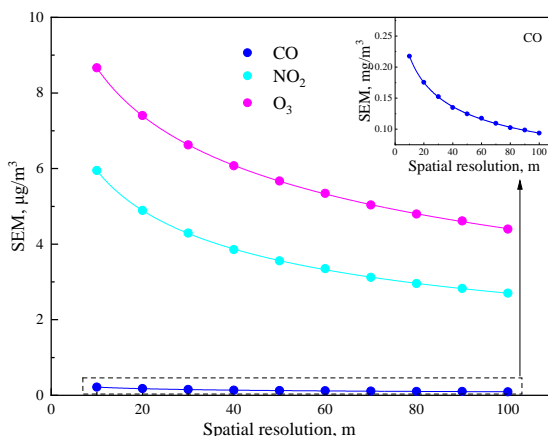


Figure 4. Relationship between grid resolution and the domain-averaged standard error of the mean of samples in each grid (SEM) for CO, NO₂, and O₃.

3.2 Road network coverage

A total of 1.32 million pieces of data were obtained during the observation period, which covers 66.4% of the major roads in Nanjing in the sampling domain with a large repeat-visit frequency [median repetition = 61 (14 and 264 as the lower and upper quartiles, respectively, the same hereinafter)] (Figure 5a). The type of road with the most visits is the Neihuan lines [258 (116, 526)], followed by the arterial roads [125 (35, 393)], secondary roads [151 (24, 442)], and highways [34 (12, 115)]. The residential streets [22 (6, 100)] have the least visits.

Apart from the areas without roads, such as the Yangtze River, Xuanwu Lake, and Purple Mountain, the data covers 43.5% of the 50-m grids in the research area with the two taxis contributing 36.8% and 37.2%. As shown in Fig 5b, the median number of repeated frequency in each grid is 66 (18, 286), with the highest value of 15449 in Nanjing South Railway Station and the lowest in some residential roads (1). The repeated frequencies in each 50-m grid along the arterial roads and Neihuan line are higher than other types of roads, i.e. Zhongyang road, Huju road, Neihuandong and Neihuanxi lines (Figure 5b). Our repeated frequency is generally higher than previous research on mobile monitoring of urban air pollution (Peters et al., 2013; Poppel et al., 2013; Bossche et al., 2015; Apte et al., 2017), which can lower the uncertainty of our results.

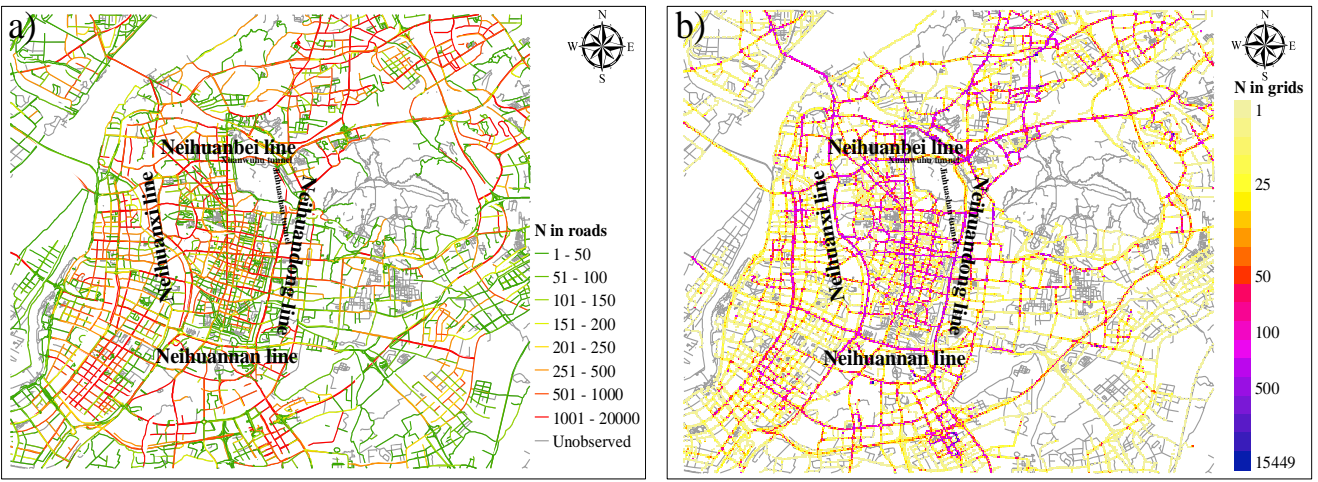


Figure 5. Mobile monitoring data coverage with regard to roads (a) and 50 m grids (b). © OpenStreetMap contributors 2019. Distributed under a Creative Commons BY-SA License.

3.3 Variability analysis

Figure 6 and Figure S1 show the coefficients of variation ($CV \equiv \text{standard deviation} / \text{mean} \times 100\%$) for different air pollutants in each grid. For one thing, this metric quantifies the sensing power of mobile monitoring, i.e. more data points reduce uncertainty of observations. For another, it reflects the inherent variability of pollutants caused by factors such as meteorological conditions and hotspots emission sources. We find that the CV values are lower than 100% on the main roads, including highways and arterial roads, but higher than 100% on some tunnel and residential streets. As discussed above, the road network coverage is much higher over the main roads than smaller roads. This indicates that increasing the sampling numbers within secondary and residential roads is the most useful to reduce the uncertainty of mobile observation. It is also interesting to notice that a single taxi has a data coverage of $\sim 37\%$ but the second one only increases it by $\sim 6\%$ to 43.5% , which implies that the marginal increase of spatial coverage decreases substantially with increasing number of sensors. This is indeed one limitation of our monitoring platform, and much larger fleet size or different sampling platforms (e.g. bikes) may be needed to reduce the uncertainty over these smaller roads.

Although the spatial patterns of CV are similar for different air pollutants, we find generally higher CV for O_3 (67.3%) and NO_2 (59.5%) than CO (51.6%). This is associated with the spatial and temporal variability of different air pollutants, which is mainly influenced by their lifetimes in the atmosphere. The chemical properties of CO are the most stable in the environment ($\tau = 1\text{--}2$ months), and its spatial concentration difference is more affected by the sampling time and the number of samples. The lifetime of NO_x is shorter ($\tau = 2\text{--}11$ hours, Romer et al., 2016), so the measured concentrations are more influenced by local or “hotspot” emissions and meteorological factors. O_3 has the shortest lifetime ($\tau = \sim 1$ hour in urban atmosphere, McClurkin et al., 2013) among the three pollutants. The level of ozone is affected by its precursors (NO_2 and VOCs), which both have large variability (Sharma et al., 2016). The complex chemical reactions also increase its spatial heterogeneity.



225

Figure 6. Spatial distribution of coefficient of variation for CO in 50 m grids in research domain. © OpenStreetMap contributors 2019. Distributed under a Creative Commons BY-SA License.

3.4 Spatial distribution

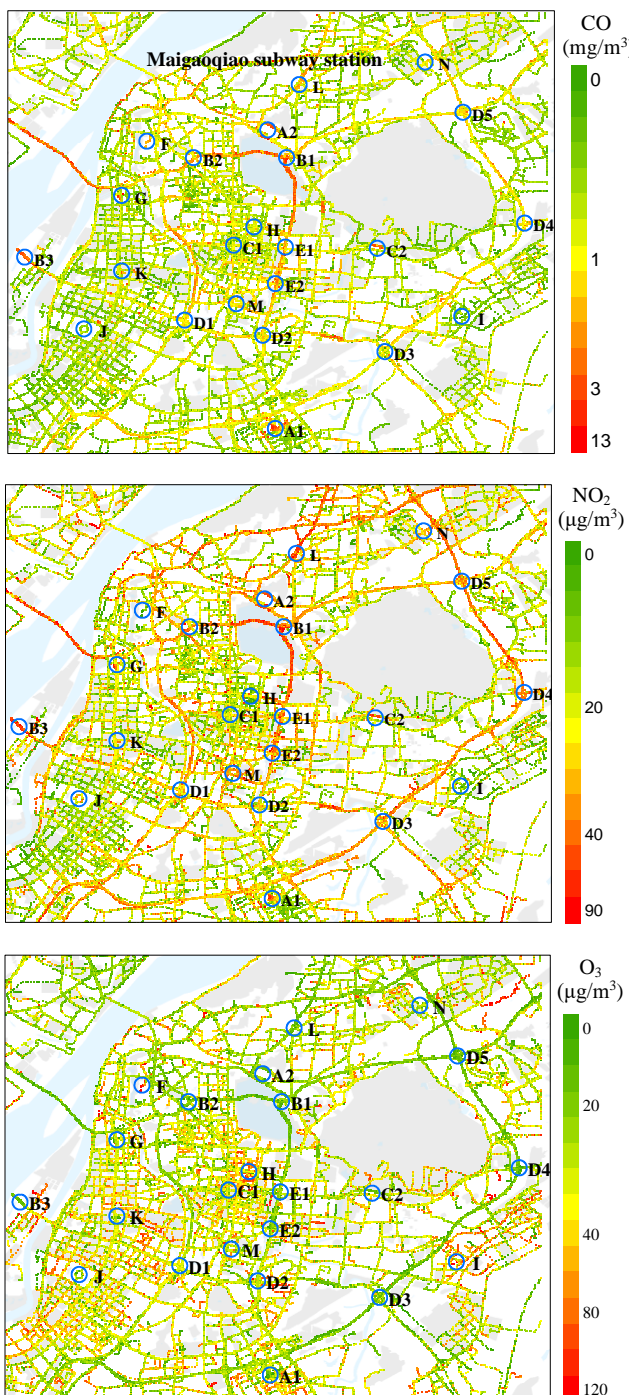
3.4.1 Hotspots identification

230 Although the instantaneous pollution level varies drastically in different road environments, we obtain a relatively robust time integrated pollution estimate by calculating the mean of repeatedly samples (Figure 7). We define the area where the pollutant concentrations are 50% higher than nearby grids (radius = 300 m) as "hotspots" following Apte et al., (2017).
 235 The pollutant concentrations shown in Table 1 are the values after deducting the background concentration, which are calculated by the annual mean concentration of stationary stations. A total of 14 hotspots are identified, and the specific information is shown in Table 1. Most of the "hotspots" show relatively apparent spatial "peaks" for multiple pollutants. To identify the main sources contributing to these hotspots, we use the different relative concentrations of the measured pollutants (Zhao et al., 2015). We also use field information around hotspots area, such as the existence of subway stations, construction sites, factories, and restaurants nearby.

240 We find that "hotspots" are mainly affected by one of the three types of emission sources, namely traffic emissions (diesel and gasoline on-road vehicle exhaust), industrial emissions, and cooking fumes. The mean CO and NO₂ concentrations are relatively high at the crossroads (E, 1.47 mg/m³ and 15.8 µg/m³), tunnels (B, 1.24 mg/m³ and 16.6 µg/m³, respectively), the roads near the hospital (M, 0.66 mg/m³ and 15.7 µg/m³), and near the railway station (A, 0.60 mg/m³ and 4.0 µg/m³), which are affected by on-road traffic emissions. In addition, due to the construction of Maigaoqiao subway station (L, 0.91 mg/m³ and 11.8 µg/m³), diesel vehicles and off-road traffic emission also make a great contribution to CO and NO₂ concentrations. Industrial emissions from petrochemical enterprises (N) also lead to high NO₂ concentrations (0.26 – 93.1 µg/m³) on surrounding roads. Cooking fumes may come from the barbecue shop (H). Due to the small number of observations, the concentrations of CO and NO₂ are relatively low, which are 0.19±0.11 µg/m³ and 3.10±9.79 µg/m³.

245 As shown in Figure 7, mean O₃ concentration in these hotspots area is different from that of CO and NO₂. The lower O₃ concentrations in these hotspots area are mainly caused by higher NOx pollution levels from the heavy traffic (Xie et al., 2016; Ding et al., 2013). Taxi sensor data also reveals the secondary pollution characteristics in micro scales, showing that O₃ concentration in the downtown area with dense buildings is significantly higher than that in other areas, especially some residential areas in Jianye and Gulou district. Previous studies have also found that the air pollutants "hotspots" are associated with traffic-related emissions [e.g., heavy-duty diesel vehicles (Targino et al., 2016) and vehicle congestion

(Gately et al., 2017)] and high-density urban areas (Li et al., 2018). These identified air pollution “hotspots” and the diagnosed source contributions provide helpful information for urban air quality management, which demonstrates the sensing power of mobile monitoring deployed on taxi fleet.



260 **Figure 7.** Spatial distribution and “hotspots” of air pollutant concentrations in the research domain (CO, NO₂, and O₃). Circles marked with A-N represent the identified “hotspots”, where the air pollutants concentrations are at least 50% higher than the surrounding area (300 m radius). © OpenStreetMap contributors 2019. Distributed under a Creative Commons BY-SA License.

Table 1. “Hotspots” of air pollution for multi-pollutants identified in Nanjing.

ID	Specific	No	CO, mg/m ³	NO ₂ , µg/m ³	Description/Potential sources
A	A1,A2	6535	0.60±0.82	4.0±15.9	Nanjing railway station, gasoline vehicle emission
B	B1,B2,B3	4177	1.24±1.74	16.6±26.1	Exit and entrance of tunnel, gasoline vehicle emission
C	C1,C2,C3	1002	0.73±0.39	0.90±12.5	Subway entrance, gasoline vehicle emission

ID	Specific	No	CO, mg/m ³	NO ₂ , µg/m ³	Description/Potential sources
D	D1-D6	4333	0.46±0.61	6.10±15.0	Overpass on ring road, vehicle emission
E	E1,E2	5354	1.47±3.04	15.8±26.8	Crossroads, vehicle emission
F	F	4664	0.28±0.71	2.30±16.5	Residential area, with higher H/W ratio
G	G	1052	0.55±0.53	13.5±14.2	Moonlight Plaza/ vehicle emission
H	H	92	0.19±0.11	3.10±9.79	Cooking emissions
I	I	4967	0.52±0.59	5.40±15.3	Nanjing Hi-Tech Industry Development Zone
J	J	4229	0.60±0.62	5.30±14.9	Olympic Sports Center, vehicle emission
K	K	3957	0.33±0.46	0.90±14.3	The memorial hall in Nanjing, vehicle emission
L	L	6160	0.91±1.31	11.8±21.0	Maigaoqiao subway station, diesel vehicle emission
M	M	6231	0.66±0.74	15.7±23.5	Hospital, vehicle emission
N	N	2386	0.36±0.49	5.60±14.0	Petrochemical enterprises, Industrial emissions

265 No: Observation points within 300 m near the hotspots.

3.4.2 Air pollutant concentrations in different types of roads

We find that air pollutant levels differ vastly among the five types of roads ($p < 0.05$, with ANOVA method). The mean CO and NO₂ concentrations follow this trend: highways (1.10 ± 0.59 mg/m³ and 29.2 ± 8.66 µg/m³, respectively) > arterial roads (0.958 ± 0.308 mg/m³ and 25.0 ± 6.90 µg/m³) > secondary roads (0.855 ± 0.401 mg/m³ and 21.8 ± 8.89 µg/m³) > branch roads (0.818 ± 0.216 mg/m³ and 20.3 ± 6.79 µg/m³) > residential streets (0.783 ± 0.299 mg/m³ and 19.7 ± 8.35 µg/m³) (Table 2). However, the mean O₃ concentrations in different types of roads are opposite to that of CO and NO₂: residential streets (35.1 ± 15.4 µg/m³) > branch roads (32.7 ± 12.2 µg/m³) > secondary roads (31.9 ± 10.0 µg/m³) > arterial roads (29.6 ± 7.52 µg/m³) > highways (23.3 ± 9.12 µg/m³).

The differences of air pollutant concentrations among different road types are firstly affected by the traffic-related emission sources including vehicle engine exhaust, which is a function of traffic flow and speed, vehicle type, etc. (Sahanavin et al., 2018). The general decreasing trends we observed for CO and NO₂ are consistent with traffic flow and congestion index in Nanjing urban area (Table 2, Zou et al., 2017). Apte et al. (2017) also found that the NO₂ concentration decreased in turn on highways, arterial roads and residential streets, which are in good agreement with our research. The observed O₃ concentrations have opposite trends of CO and NO₂ with highest concentrations in residential streets (Table 2). As O₃ production in Nanjing is in VOC-limited regions, lower NO_x could reduce its titration of O₃ and subsequently increase O₃ concentrations (Ding et al., 2013; Xie et al., 2016). This indicates the necessity of VOC emission control to reduce O₃ pollution in urban areas of Nanjing. The O₃ concentrations are also lower in tunnels, which is associated with the lack of sunlight in the tunnel.

Table 2. Multi-pollutant concentrations in five types of roads.

Road types	Road numbers	Vehicle speed, km/h	Traffic congestion index ^a	CO, mg/m ³	NO ₂ , µg/m ³	O ₃ , µg/m ³
Highways	168	60~80	2.18	1.10 ± 0.594	29.2 ± 8.66	23.3 ± 9.12
Arterials	443	40~60	1.78	0.958 ± 0.309	25.0 ± 6.90	29.7 ± 7.53
Secondary	419	30~50	1.70	0.855 ± 0.401	21.8 ± 8.89	31.9 ± 10.0
Branch roads	349	20~40	-	0.818 ± 0.216	20.3 ± 6.79	32.7 ± 12.2
Residential	152	< 20	-	0.783 ± 0.230	19.6 ± 8.35	35.1 ± 15.5

285 a: The traffic congestion index data is from Gaud map <https://report.amap.com/detail.do?city=320100>.

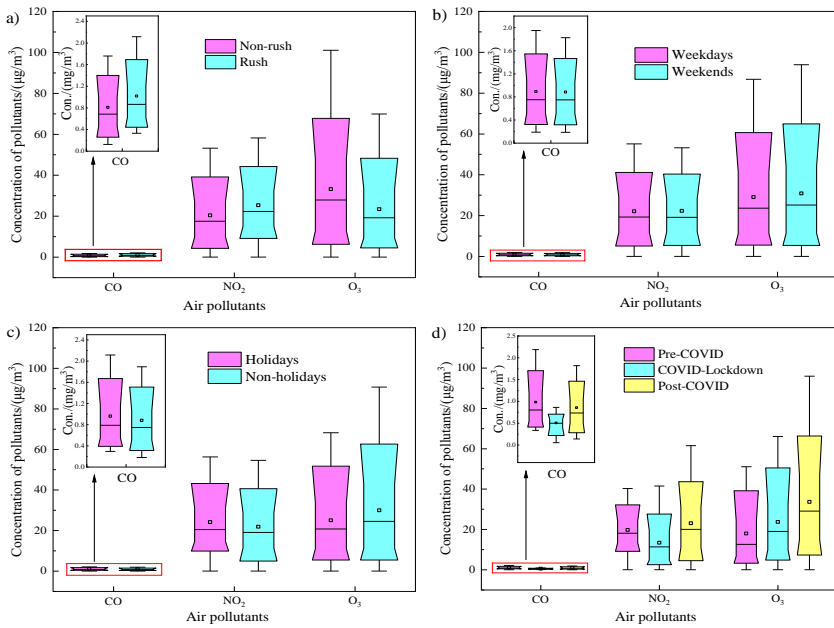
3.5 Temporal variation

Figure 8 shows the temporal variation of the three air pollutant concentrations during the observation campaign, with

the hourly mean concentrations over the research domain shown in Figure 9 (the corresponding spatial distributions are shown in Figure S3-5). The difference of the hourly variation of the mean sample of different types of roads over a year is small (Figure S6), so the data in Figure 9 is not filtered in anyway, but for each hour have a similar mix of road types sampled. We find that the median concentrations of CO and NO₂ in rush hours (7-9 A.M and 5-7 P.M) are increased by 26.4% and 27.3% compared to non-rush hours, respectively. The hourly mean concentrations of CO and NO₂ show a double-peak pattern with higher concentrations in rush hours (Figure 9a), reflecting the contribution of traffic-related emissions (Tan et al., 2009), which we will elaborate in next section. The observed O₃ concentrations show a unimodal diurnal pattern with a peak at ~2 P.M as a result of photochemical formation. At night, O₃ concentrations are maintained at a low level due to no solar radiation and NOx titration (Xie et al., 2016; Li et al., 2013). These patterns generally agree with the measurements at stationary monitoring stations (Figure S2).

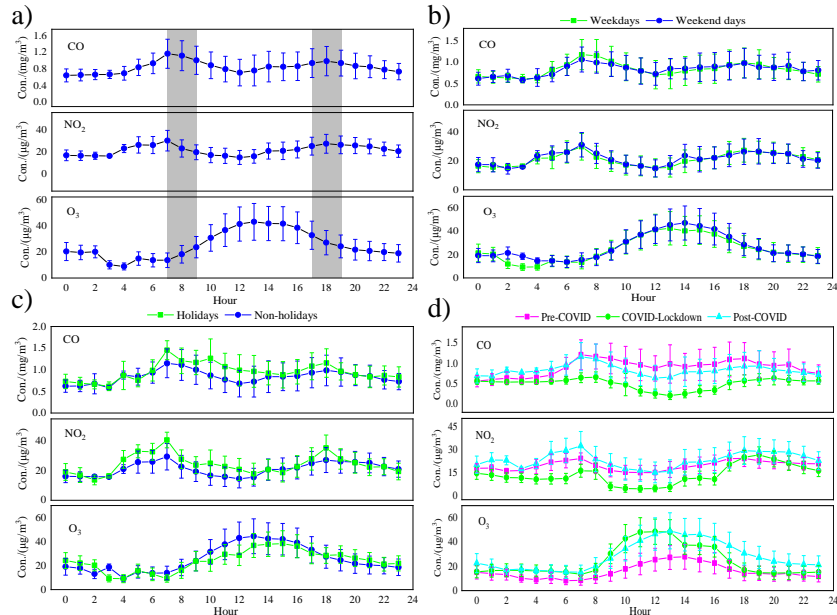
No significant differences are observed for the median concentrations and spatial distribution of three air pollutants between weekdays and weekends ($\alpha = 0.05$, Figure 8b and S4), even though the morning peaks for CO is slightly higher during weekdays (Figure 9b), which is consistent with An et al. (2015). Wang et al. (2013) found that NOx displays weekly cycle in the Beijing–Tianjin–Hebei metropolitan area, with higher level on weekdays than weekends. Qin et al. (2004) observed a significant weekend effect in southern California, showing that in the morning traffic rush time, the concentrations of CO and NO₂ at weekends were about 18% and 37% lower than on weekdays. The difference between our study and other cities lies in the difference of fleet fuel structure, and the different weekly routine of human activities and the taxi driving trajectories (Xie et al., 2016).

The median concentrations of CO and NO₂ during holidays are comparable to those in non-holidays, but are 18.3% lower for O₃ (Figure 8c). In addition, compared with the spatial distribution of O₃ concentration in holidays, we find that the concentrations of O₃ in Xinjiekou and its surrounding areas, where many shopping malls are located, are higher in non-holidays (Figure S5). This may be related to the higher NO₂ concentrations in this area during holidays ($24.8 \pm 10.2 \mu\text{g}/\text{m}^3$) than non-holidays ($20.6 \pm 4.82 \mu\text{g}/\text{m}^3$). The hourly concentrations show no significant difference between holidays and non-holidays (Figure 9c). The holidays include the periods of National Day (Oct. 1-7), the Spring Festival (Feb. 24-31), Qingming Festival (Apr. 4-6), international labor day (May. 1-5), and the Dragon Boat Festival (Jun. 25-27). “Holiday effect” has been observed extensively for urban and regional air quality. For example, Xu et al. (2017) found that VOC tracers were significantly enhanced during the National Day holiday (from Oct 1 to Oct 10, 2014) in Yangtze River Delta (YRD) region, indicating that the “holiday effect” had a strong influence on the distribution and chemical reactivity of VOC in the atmosphere. The reason why this effect is not observed in this study may be related to the relatively smaller sample size during holidays. The sample size for holidays account for only 11.3% of those for the non-holidays.



320

Figure 8. Variation of pollutants concentrations in rush/non-rush hours, weekdays/weekend days, holidays/non-holidays, and three stages of the COVID-19 pandemic. The dot in each box represents the mean value and the solid line represents the median value. Each box extends from the 25th to the 75th percentile. The whiskers (error bars) below and above the boxes represents the 10th and 90th percentiles.



325

Figure 9. Diurnal cycles of three pollutants concentrations measured in rush/non-rush hours, weekdays/weekend days, holidays/non-holidays, and different stage of the COVID-19 pandemic by the taxi sensors. Error bars in panel a show the standard deviation of observations. Gray areas represent the rush hours, and the other represents the non-rush hours (a).

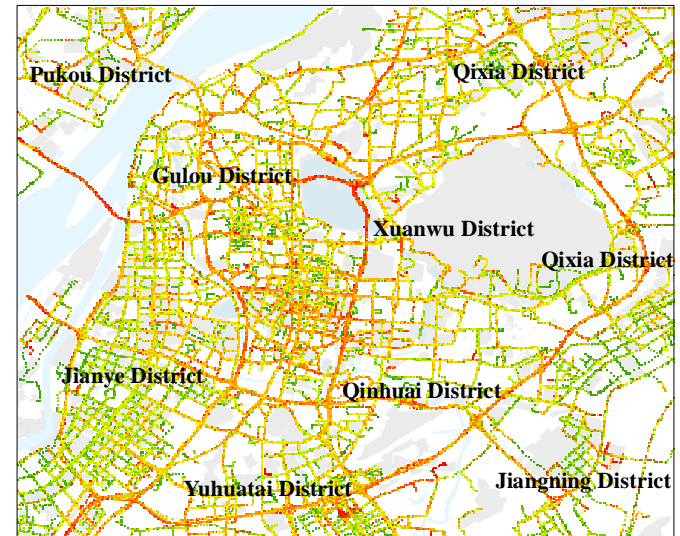
3.6 Traffic source contribution

Figure 10a and 10b show the calculated contributions by traffic-related sources to the observed concentrations of CO (referred to as contributions hereinafter). We find that the mean contribution calculated by BS method ($42.6 \pm 11.5\%$) is 330 generally consistent with that obtained from PD algorithm ($43.9 \pm 27.0\%$). Their spatial patterns are also similar (Figure 10a vs 10b). The contributions in highways, near tunnel entrances and exits (e.g. Jiuhuashan and Xuanwuhu tunnel), railway station (Nanjing south station), and arterial roads (44-59%) calculated by the both methods are higher than secondary roads, residential streets, and lowest in branch roads (29-39%) (Table 3), which is consistent with the trends in traffic volumes. The patterns for NO₂ are quite similar to CO (Figure S7c and S7d, Table 1), but the mean contribution to NO₂ calculated by BS method ($26.3 \pm 14.7\%$) is lower than that obtained from PD algorithm ($40.2 \pm 29.9\%$). This difference is associated with the 335

relatively higher uncertainty for NO_2 measurements by sensors (Section 2.2), while the results of PD method seem unaffected as the sensor bias are cancelled when calculating the difference between “peak” and “basement” (Section 2.4).

Bottom-up emission inventory indicates that on-road transportation contributed ~11% of total CO emissions from Nanjing in 2012 (Zhao et al., 2015). Considering the number of cars has increased ~80% and the total CO emissions remained relatively stable (BSNM, 2019), the contribution of traffic sources in recent years is expected to be ~20%. These values are much lower than what we calculated based on mobile monitoring data because of the lower spatial resolution of these regional inventories (e.g. $0.05^\circ \times 0.05^\circ$) (Zheng et al., 2014). They are unable to distinguish the emission characteristics of air pollutants within a street level (tens of meters), which leads to their underestimation of traffic-related emissions in the road micro-environment.

a), CO, BS method, %



b), CO, PD method, %

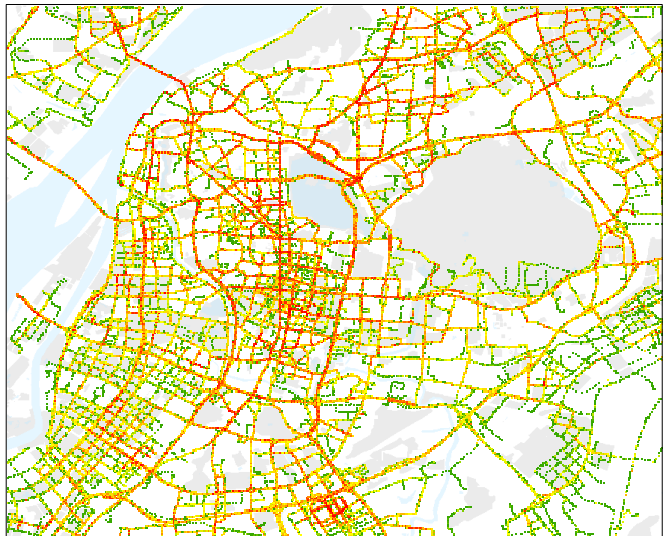


Figure 10. Contributions from traffic-related emissions calculated by stationary data method (a) and peak detection algorithm (b) for CO. © OpenStreetMap contributors 2019. Distributed under a Creative Commons BY-SA License.

Table 3. Contribution of traffic emissions to CO and NO_2 in different roads by two methods.

Road types	Traffic emission - CO, %		Traffic emission - NO_2 , %	
	BS	PD	BS	PD
Highways	48.3 ± 10.4	51.0 ± 20.4	32.5 ± 14.5	41.4 ± 22.5
Arterials	44.1 ± 9.23	59.0 ± 19.4	26.8 ± 10.6	43.6 ± 23.3
Secondary	40.2 ± 11.7	47.6 ± 23.9	22.8 ± 13.2	35.2 ± 25.1
Residential	39.4 ± 14.1	38.9 ± 26.1	20.3 ± 16.3	28.6 ± 25.0
Branch roads	39.2 ± 12.2	29.7 ± 23.9	21.5 ± 18.1	25.5 ± 24.4

3.7 Impact of COVID-19 pandemic

Figure 8d and 9d show the variation of air pollutant concentrations in different stages of the COVID-19 pandemic. The spatial distributions of concentrations and traffic contributions are also depicted in Figure 11-12 and Figure S8-S9. We divide the data into three stages: Pre-COVID (P1, Oct. 1, 2019 – Jan. 23, 2020), COVID-Lockdown (P2, Jan. 24 – 31, 2020 and Feb. 17 – 24, 2020), and Post-COVID (P3, Mar. 1, 2020 – Sep. 30, 2020). We find the median concentrations of CO and NO_2 were the lowest in P2 (Figure 9d). For example, the CO and NO_2 concentrations decreased by 44.9% and 41.7% from P1 to P2, respectively (Figure 11 and S8). This pattern agrees well with the air quality station data over eastern China (Huang et al.,

2020). We focus on the traffic sector as it is the most sensitive to lockdown measures, while other sectors, including power, industrial and residential sectors, remain relatively unchanged (Guevara et al., 2020). We find that from P1 to P2, the average traffic source contributions of CO and NO₂ by BS method decreased by 59.9% and 51.8%, respectively (Figure 12 and S9). This is consistent with the transportation index data, which shows a 70% reduction in eastern China cities during lockdown (Huang et al. 2020).

The observed CO and NO₂ concentrations recovered to levels similar to P1 during P3. The traffic-related source contributions were increased by 120% and 131% from P2 to P3 for CO and NO₂ (Figure 11 and S9). Due to the limited data size and spatial coverage (only in some arterial roads and highways) during P2, the calculated contributions of traffic emissions to air pollutants may be not directly comparable to those shown in Figure 9. But the changes of the contributions well track the change of traffic volume and human activities (Bao and Zhang, 2020). Our results also agree with top-down emission estimates from remote sensing data (Zhang et al. 2020), which showed the total NO₂ emissions decreased by 31-44% from P1 to P2, but increased 67-85% from P2 to P3.

The observed ozone concentrations show a different trend from other pollutants in the three stages. We find a pattern of P1 < P2 < P3 for O₃ median concentrations (Figure 8d). The ozone concentrations increased by 35.7% from P1 to P2, and 48.7% from P2 to P3 (Figure S8). While the contribution of traffic emissions to ozone first decreased by 32.5% from P1 to P2 period, and then increased by 39.3% in P2 to P3 period (Figure S9). This is firstly associated with the less titration of NO_x during P2 as discussed earlier. In addition, the increased temperature and solar insolation in P2 and P3 also favor the photochemical formation of O₃ than in P1 (Xie et al., 2016; Fu et al., 2015; Reddy et al., 2010).

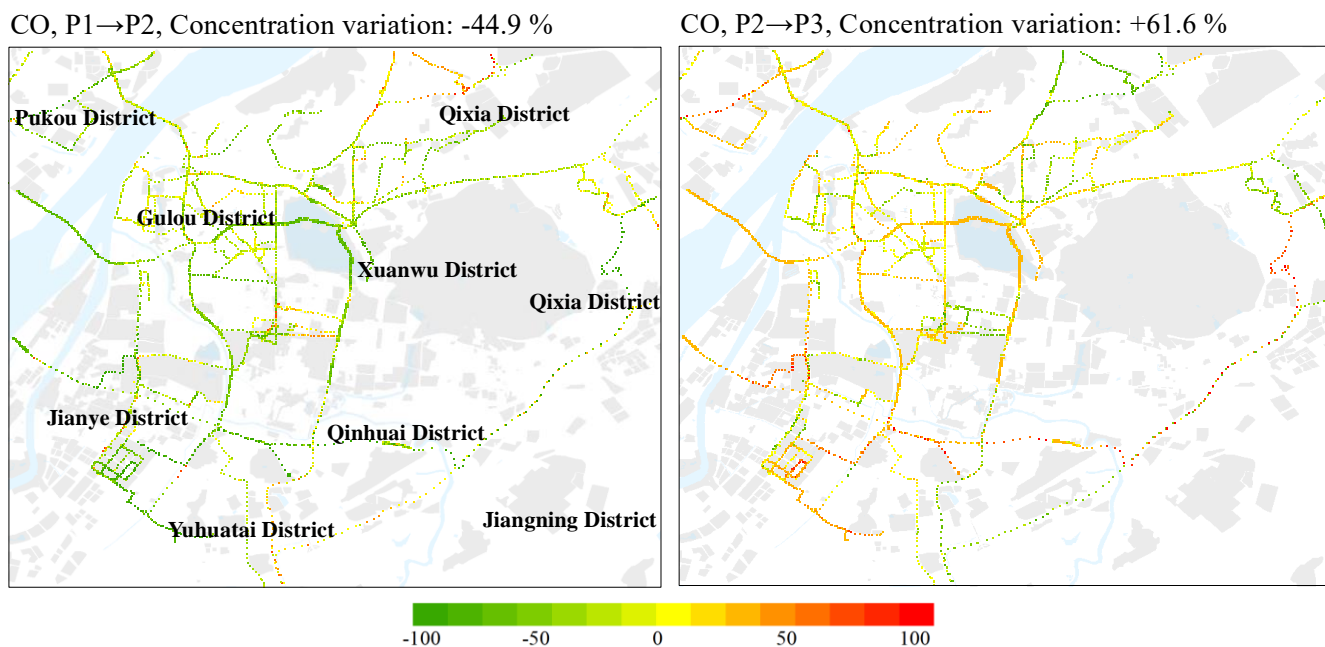


Figure 11. Changes of observed CO concentration in the three stages of the COVID-19 pandemic. P1, P2, and P3 are for pre-COVID, COVID-Lockdown, and post-COVID periods, respectively. © OpenStreetMap contributors 2019. Distributed under a Creative Commons BY-SA License.

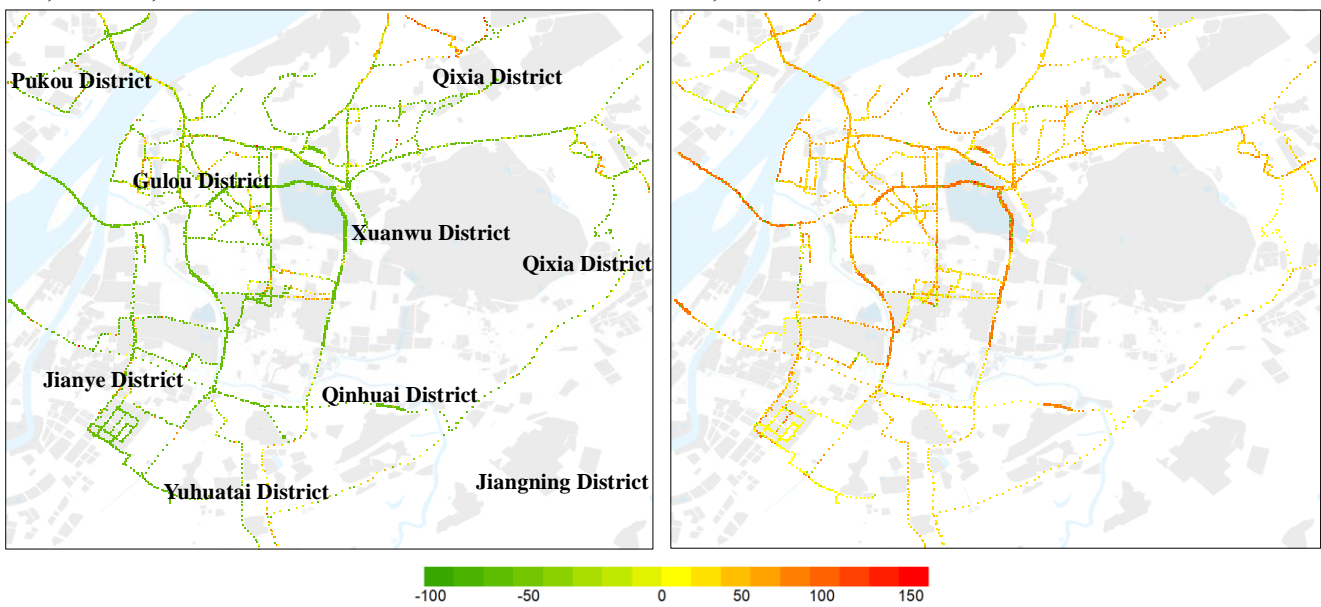


Figure 12. Changes of the contributions of traffic-related sources to CO in the three stages of the COVID-19 pandemic calculated by BS method. P1, P2, and P3 are for pre-COVID, COVID-Lockdown, and post-COVID periods, respectively. © OpenStreetMap contributors 2019. Distributed under a Creative Commons BY-SA License.

385

4 Conclusions

To accurately assess human exposure to urban air pollution requires a detailed understanding of the spatial and temporal patterns of air pollutant concentrations. Combined mobile monitoring with GIS technology, we obtained high-resolution (50m×50m) spatial distribution maps of three air pollutants in the main urban area of Nanjing, which well demonstrates the spatial heterogeneity of pollutants at the micro-scales. We find that higher spatial resolutions are useful to identify hotspots that are mainly affected by five types of air pollution source emissions, namely, traffic, industrial, dust, and cooking fumes. It also provides hints for air quality management and emission source control.

We calculate the contribution of traffic-related emissions to air pollutants in different grid points by combining mobile observation and station observation data. Compared with the peak detection method, the station data method is more reasonable for secondary pollutants as O_3 , while the former is less affected by sensor bias. There are also differences in the contribution of traffic emissions to air pollutants in different types of roads. Due to the impact of the COVID-19 pandemic, the mean concentrations of CO and NO_2 decreased by 44.9% and 47.1%, respectively, during the lockdown in Nanjing, and the contribution of traffic-related emissions also decreased by 59.9% and 52.6%. On the contrary, the concentration of O_3 increased by 35.7%, respectively. After reopening, CO and NO_2 concentrations rebounded by 61.6% and 48.2%, and the contribution of traffic emissions both increased over 100%, indicating the great impact of traffic emissions on urban air pollution.

Data availability

All validation data and data processing by GIS used in this work are accessed by contacting the authors.

405

Author contribution

YZ designed the research; SW performed the research; SW, YZ, ZW, and MY analyzed data; LW, XC, and AD provided validation data; MY, YL, and QL helped data analysis; MW, LZ, and YX provided monitoring instrument; SW and YZ wrote the paper.

Competing interests

The authors declare that they have no conflict of interest.

Acknowledgments

This study was supported by the National Key R&D Program of China (2019YFA0606803), Start-up fund of the Thousand Youth Talents Plan, Jiangsu Innovative and Entrepreneurial Talents Plan, and the Collaborative Innovation Center of Climate Change, Jiangsu Province. The authors thank Rong Ye and Liang Luo for sample collection.

References

Airparif.: Influence des aménagements de voirie sur l'exposition des cyclistes a la pollution atmosphérique; Study report Airparif: Paris, France, 2009.

An, J. L., Zou, J., Wang, J., Lin., X., and Zhu, B.: Differences in ozone photochemical characteristics between the megacity Nanjing and its suburban surroundings, Yangtze River Delta, China, *Environ. Sci. Pollut. Res.*, 22, 19607–19617, <https://doi.org/10.1007/s11356-015-5177-0>, 2015.

Apte, J. S., Kirchstetter, T. W., Reich, A. H., Deshpande, S. J., Kaushik, G., Chel, A., Marshall, J. D., and Nazaroff, W. W.: Concentrations of fine, ultrafine, and black carbon particles in auto-rickshaws in New Delhi, India, *Atmos. Environ.*, 45, 4470-4480, <https://doi.org/10.1016/j.atmosenv.2011.05.028>, 2011.

Apte, J. S., Messier, K. P., Gani, S., Brauer, M., Kirchstetter, T. W., Lunden, M. M., Marshall, J. D., Portier, C. J., Vermeulen, R. C. H., and Hamburg, S. P.: High-resolution air pollution mapping with google street view cars: exploiting big data, *Environ. Sci. Technol.*, 51, 6999-7008, <https://doi.org/10.1021/acs.est.7b00891>, 2017.

Bao, R. and Zhang, A.: Does lockdown reduce air pollution? Evidence from 44 cities in northern China, *Sci. Total Environ.*, 139052, <https://doi.org/10.1016/j.scitotenv.2020.139052>, 2020.

Bart, E., Jan P., Martine, V. P., Nico, B., and Arnout, S.: The aeroflex: a bicycle for mobile air quality measurements, *Sensors*, 13(1), 221-240, <https://doi.org/10.3390/s130100221>, 2012.

Boogaard, H., Kos, G. P. A., Weijers, E. P., Janssen, N. A. H., Fischer, P. H., Van der Zee, S. C., De Hartog, J. J., and Hoek, G.: Contrast in air pollution components between major streets and background locations: Particulate matter mass, black carbon, elemental composition, nitrogen oxide and ultrafine particle number, *Atmos. Environ.*, 45, 650-658, <https://doi.org/10.1016/j.atmosenv.2010.10.033>, 2010.

Borrego, C., Coutinho, M., Costa, A. M., Ginja, J., Ribeiro, C., Monteiro, A., Ribeiro, I., Valente, J., Amorim, J. H., Martins, H., Lopes, D., and Miranda, A. I.: Challenges for a new air quality directive: the role of monitoring and modelling techniques, *Urban Climate*, 14 (3), 328-341, <https://doi.org/10.1016/j.uclim.2014.06.007>, 2015.

Bossche, J. V. D., Peters, J., Verwaeren, J., Botteldooren, D., Theunis, J., and Baets, B. D.: Mobile monitoring for mapping spatial variation in urban air quality: Development and validation of a methodology based on an extensive dataset, *Atmos. Environ.*, 105, 148-161, <https://doi.org/10.1016/j.atmosenv.2015.01.017>, 2015.

Bureau Statistics of Nanjing Municipal.: Nangjing Statistical Yearbook. <http://tjj.nanjing.gov.cn/bmfw/njsj/>, 2019.

Castell, N., Dauge, F. R., Schneider, P., Vogt, M., Lerner, U., Fishbain, B., Broday, D., and Bartonova, A.: Can commercial low-cost sensor platforms contribute to air quality monitoring and exposure estimates? *Environ. Int.*, 99, 293-302, <https://doi.org/10.1016/j.envint.2016.12.007>, 2017.

Cavellin, L. D., Weichenthal, S., Tack, R., Ragettli, M. S., Smargiassi, A., and Hatzopoulou, M.: Investigating the use of portable air pollution sensors to capture the spatial variability of traffic-related air pollution, *Environ. Sci. Technol.*, 50, 313-320, <https://doi.org/10.1021/acs.est.5b04235>, 2016.

Chatzidiakou, L., Krause, A., Popoola1, O. A. M., Antonio1, A.D., Kellaway, M., Han, Y.Q., Squires, F. A., Wang, T., Zhang,

450 H. B., Wang, Q., Fan, Y. F., Chen, S. Y., Hu, M., Quint, J. K., Barratt, B., Kelly, F. J., Zhu, T., and Jones, R. L.: Characterising low-cost sensors in highly portable platforms to quantify personal exposure in diverse environments, Atmos. Meas. Tech., 12, 4643-4657, <https://doi.org/10.5194/amt-12-4643-2019>, 2019.

455 Ding, A. J., Fu, C. B., Yang, X. Q., Sun, J. N., Zheng, L. F., Xie, Y. N., Herrmann, E., Nie, W., Petäjä, T., Kerminen, V. -M., and Kulmala M.: Ozone and fine particle in the western Yangtze River Delta: an overview of 1 yr data at the SORPES station, Atmos. Chem. Phys., 13, 5813-5830, <https://doi.org/10.5194/acp-13-5813-2013>, 2013.

460 Esposito, E., Vito, S. D., Salvato, M., Fattoruso, G., Bright, V., Jones, R. L., and Popoola, O.: Stochastic comparison of machine learning approaches to calibration of mobile air quality monitors, Sensors Cham., 294-302, https://doi.org/10.1007/978-3-319-55077-0_38, 2018.

465 Farrell, W. J., Cavellin, L. D., Weichenthal, S., Goldberg, M., and Hatzopoulou, M.: Capturing the urban canyon effect on particle number concentrations across a large road network using spatial analysis tools, Build. Environ., 92, 328-334, <https://doi.org/10.1016/j.buildenv.2015.05.004>, 2015.

470 Fu, T. M., Zheng, Y., Paulot, F., and Mao, J.: Positive but variable sensitivity of August surface ozone to large-scale warming in the southeast United States, Nature Clim. Change, 5, 454-458, <https://doi.org/10.1038/nclimate2567>, 2015.

475 Gately, C. K., Hutyra, L. R., Peterson, S., and Wing, I. S.: Urban emissions hotspots: Quantifying vehicle congestion and air pollution using mobile phone GPS data, Environ. Pollut., 229, 496-504, <https://doi.org/10.1016/j.envpol.2017.05.091>, 2017.

480 Guevara, M., Jorba, O., Soret, A., Petetin, H., Bowdalo, D., Serradell, K., Tena, C., Van der Gon, H. D., Kuenen, J., Peuch, V. H., and Garc á-Pando, C. P.: Time-resolved emission reductions for atmospheric chemistry modelling in Europe during the COVID-19 lockdowns, Atmos. Chem. Phys., <https://doi.org/10.5194/acp-2020-686>, 2020.

485 Hagan, D. H., Gani, S., Bhandari, S., Patel, K., Habib, G., Apte, J. S., Ruiz, L. H., and Kroll, J. H.: Inferring aerosol sources from low-cost air quality sensor measurements: a case study in Delhi, India, Environ. Sci. Technol. Lett., 6, 467-472, <https://doi.org/10.1021/acs.estlett.9b00393>, 2019.

490 Hasenfratz, D., Saukh, O., Walser, C., Hueglin, C., Fierz, M., Arn, T., Beutel, J., and Thiele, L.: Deriving high-resolution urban air pollution maps using mobile sensor nodes, Pervasive and Mobile Computing, 16, 268-285, <https://doi.org/10.1016/j.pmcj.2014.11.008>, 2015.

495 Hilker, N., Wang, J. M., Jeong, C., Healy, R. M., Sofowote, U., Debosz, J., Su, Y., Noble, M., Munoz, A., Doerksen, G., White, L., Audette, C., Herod, D., Brook, J. R., and Evans, G. J.: Traffic-related air pollution near roadways: discerning local impacts from background, Atmos. Meas. Tech., 12, 5247-5261, <https://doi.org/10.5194/amt-12-5247-2019>, 2019.

500 Huang, X., Ding, A. J., Gao, J., Zheng, B., Zhou, D. R., Qi, X., Tang, R., Wang, J., Ren, C., Nie, W., Chi, X., Xu, Z., Chen, L., Li, Y., Che, F., Pang, N., Wang, H. K., Tong, D., Qin, W., Cheng, W., Liu, W., Fu, Q., Liu, B., Chai, F. H., Davis, S. J., Zhang, Q., and He, K. B.: Enhanced secondary pollution offset reduction of primary emissions during COVID-19 lockdown in China, Natl. Sci. Rev., <https://doi.org/10.1093/nsr/nwaa137>, 2020.

505 Isakov, V., Touma, J. S., and Khlystov, A.: A method of assessing air toxics concentrations in urban areas using mobile platform measurements, J. Air Waste Manage. Assoc., 57(11), 1286-1295, <https://doi.org/10.3155/1047-3289.57.11.1286>, 2007.

510 Johnson, N. E., Bonczak, B., and Kontokosta, C. E.: Using a gradient boosting model to improve the performance of low-cost aerosol monitors in a dense, heterogeneous urban environment, Atmos. Environ., 184, 9-16, <https://doi.org/10.1016/j.atmosenv.2018.04.019>, 2018.

515 Kaivonen, S. and Ngai, E.: Real-time air pollution monitoring with sensors on city bus, Digit. Commun. Netw., 6, 23-30, <https://doi.org/10.1016/j.dcan.2019.03.003>, 2020.

520 Karner, A. A., Eisinger, D. S., and Niemeier, D. A.: Near-roadway air quality: synthesizing the findings from real-world data, Environ. Sci. Technol., 44(14), 5334-5344, <https://doi.org/10.1021/es100008x>, 2010.

Kaur, S., Nieuwenhuijsen, M. J., and Colvile, R. N.: Fine particulate matter and carbon monoxide exposure concentrations in urban street transport microenvironments, *Atmos. Environ.*, 41, 4781-4810,

495 <https://doi.org/10.1016/j.atmosenv.2007.02.002>, 2007.

Kerckhoffs, J., Hoek, G., Messier, K. P., Brunekreef, B., Melfi, K., Klompmaker, J. O., and Vermeulen, R.: Comparison of ultrafine particle and black carbon concentration predictions from a mobile and short-term stationary land-use regression model, *Environ. Sci. Technol.*, 50(23), 12894-12902, <https://doi.org/10.1021/acs.est.6b03476>, 2016.

Laughner, J. L., Zhu, Q., and Cohen, R. C.: The berkeley high resolution tropospheric NO₂ product, *Earth Syst. Sci., Data* 500 10, 2069-2095, <https://doi.org/10.5194/essd-10-2069-2018>, 2018.

Le, D. K. and Cha, S. K.: Real-time air pollution prediction model based on spatiotemporal big data, *Computers and Society*, <https://arxiv.org/ftp/arxiv/papers/1805/1805.00432.pdf>, 2018.

Li, M. J., Chen, D. S., Cheng, S. Y., Wang, F., Li, Y., Zhou, Y., and Lang, J. L.: Optimizing emission inventory for chemical transport models by using genetic algorithm, *Atmos. Environ.*, 44(32), 3926-3934, 505 <https://doi.org/10.1016/j.atmosenv.2010.07.010>, 2010.

Li, Y., Lau, A.K.H., Fung, J. C. H., Zheng, J. Y., and Liu, S.: Importance of NO_x control for peak ozone reduction in the Pearl River Delta region, *J. Geophys. Res. Atmos.*, 118, 9428-9443, <https://doi.org/10.1002/jgrd.50659>, 2013.

Li, Z., Fung, J. C. H., and Lau, A. K. H.: High spatiotemporal characterization of on-road PM_{2.5} concentrations in high-density urban areas using mobile monitoring, *Build. Environ.*, 143, 196-205, 510 <https://doi.org/10.1016/j.buildenv.2018.07.014>, 2018.

Lim, C. C., Kim, H., Vilcassim, M. J. R., Thurston, G. D., Gordon, T., Chen, L. C., Lee, K., Heimbinder, M., and Kim, S.: Mapping urban air quality using mobile sampling with low-cost sensors and machine learning in Seoul, South Korea, *Environ. Int.*, 131, 105022, <https://doi.org/10.1016/j.envint.2019.105022>, 2019.

515 Maag, B., Zhou, Z., and Thiele, L.: A Survey on Sensor Calibration in Air Pollution Monitoring Deployments, *IEEE Internet of Things*, 5(6), 4857-4870, doi: 10.1109/JIOT.2018.2853660, 2018.

McClurkin, J. D., Maier, D. E., and Ileleji, K. E.: Half-life time of ozone as a function of air movement and conditions in a sealed container, *Journal of Stored Products Research*, 55, 41-47, <https://doi.org/10.1016/j.jspr.2013.07.006>, 2013.

Miller, D. J., Actkinson, B., Padilla, L., Griffin, R. J., Moore, K., Lewis, P. G. T., Gardner-Frolick, R., Craft, E., Portier, C. J., Hamburg, S. P., and Alvarez, R.A.: Characterizing elevated urban air pollutant spatial patterns with mobile monitoring in 520 Houston, Texas, *Environ. Sci. Technol.*, 54(4), 2133-2142, <https://doi.org/10.1021/acs.est.9b05523>, 2020.

Ministry of Ecology and Environment of the People's Republic of China.: 2018 China Vehicle Environmental Management Annual Report. retrieved from http://www.mee.gov.cn/xxgk2018/xxgk/xxgk15/201806/t20180601_630215.html, 2018.

Miskell, G., Salmond, J., and Williams, D. E.: A solution to the problem of calibration of low-cost air quality measurement sensors in networks, *Acs. Sensors*, 3, 832-843, <https://doi.org/10.1021/acssensors.8b00074>, 2018.

525 OpenStreetMap contributors: Roads and land use data of Nanjing retrieved from

<https://download.geofabrik.de/asia/china.html>, <https://www.openstreetmap.org>, 2020.

Padro-Martinez, L. T., Patton, A. P., Trull, J. B., Zamore, W., Brugge, D., and Durant, J. L.: Mobile monitoring of particle number concentration and other traffic-related air pollutants in a near-highway neighborhood over the course of a year, *Atmos. Environ.*, 61, 253-264, <https://doi.org/10.1016/j.atmosenv.2012.06.088>, 2012.

530 Peters, J., Theunis, J., Van Poppel, M., and Berghmans, P.: Monitoring PM₁₀ and ultrafine particles in urban environments using mobile measurements, *Aerosol Air Qual. Res.*, 13, 509-522, <https://doi.org/10.4209/aaqr.2012.06.0152>, 2013.

Poppel, M. V., Peters, J., and Bleux, N.: Methodology for setup and data processing of mobile air quality measurements to assess the spatial variability of concentrations in urban environments, *Environ. Pollut.*, 183, 224-233, 535 <https://doi.org/10.1016/j.envpol.2013.02.020>, 2013.

Qin, X., Hou, L., Gao, J., and Si, S.: The evaluation and optimization of calibration methods for low-cost particulate matter

540 sensors: Inter-comparison between fixed and mobile methods, *Sci. Total Environ.*, 715, 136791, <https://doi.org/10.1016/j.scitotenv.2020.136791>, 2020.

545 Qin, Y., Tonnesen, G. S., and Wang, Z.: Weekend/weekday differences of ozone, NO_x, CO, VOCs, PM₁₀ and the light scatter during ozone season in southern California, *Atmos. Environ.*, 38(19), 3069-3087, <https://doi.org/10.1016/j.atmosenv.2004.01.035>, 2004.

550 Reddy, B. S. K., Kumar, K. R., Balakrishnaiah, G., Gopal, K. R., Reddy, R.R., Ahammed, Y. N., Narasimhulu, K., Reddy, L. S. S., and Lal, S.: Observational studies on the variations in surface ozone concentration at Anantapur in southern India, *Atmos. Res.*, 98, 125-139, <https://doi.org/10.1016/j.atmosres.2010.06.008>, 2010.

555 Romer, P. S., Duffey, K. C., Wooldridge, P. J., Allen, H. M., Ayres, B. R., Brown, S. S., Brune, W. H., Crounse, J. D., Gouw, J. D., Draper, D. C., Feiner, P. A., Fry, J. L., Goldstein, A. H., Koss, A., Misztal, P. K., Nguyen, T. B., Olson, K., Teng, A. P., Wennberg, P. O., Wild, R. J., Zhang, L., and Cohen, R. C.: The lifetime of nitrogen oxides in an isoprene-dominated forest, *Atmos. Chem. Phys.*, 16, 7623-7637, <https://doi.org/10.5194/acp-16-7623-2016>, 2016.

560 Sharma, S., Sharma, P., Khare, M., and Kwatra, S.: Statistical behavior of ozone in urban environment, *Sust. Environ. Res.*, 26 (3), 142-148, <https://doi.org/10.1016/j.serj.2016.04.006>, 2016.

565 Shiva, N. S. M., Pavan, R.Y., Narayana, M. V., Seema, K., and Pooja, R.: Mobile monitoring of air pollution using low cost sensors to visualize spatio-temporal variation of pollutants at urban hotspots, *Sustainable Cities and Society*, 44, 520-535, <https://doi.org/10.1016/j.scs.2018.10.006>, 2019.

570 Snyder, E. G., Watkins, T. H., Solomon, P. A., Thoma, E. D., Williams, R. W., Hagler, G. S. W., Shelow, D., Hindin, D. A., Kilaru, V. J., and Preuss, P. W.: The changing paradigm of air pollution monitoring, *Environ. Sci. Technol.*, 47 (20), 11369-11377, <https://doi.org/10.1021/es4022602>, 2013.

575 Spinelle, L., Gerboles, M., Villani, M., Aleixandre, M., and Bonavitacola, F.: Field calibration of a cluster of low-cost commercially available sensors for air quality monitoring. Part B: NO, CO and CO₂, *Sensors Actuators B Chem.*, 238, 706-715, <https://doi.org/10.1016/j.snb.2016.07.036>, 2017.

580 Tan, P. H., Chou, C., Liang, J. Y., Chou, C. C. K., and Shiu, C. J.: Air pollution “holiday effect” resulting from the Chinese New Year, *Atmos. Environ.*, 43(13), 2114-2124, <https://doi.org/10.1016/j.atmosenv.2009.01.037>, 2009.

585 Targino, A. C., Gibson, M. D., Krecl, P., Rodrigues, M. V. C., Santos, M. M. D., and Corrêa, M. D. P.: Hotspots of black carbon and PM_{2.5} in an urban area and relationships to traffic characteristics, *Environ. Pollut.*, 218, 475-486, <https://doi.org/10.1016/j.envpol.2016.07.027>, 2016.

590 Vito, S. D., Esposito, E., Salvato, M., Popoola, O., Formisano, F., Jones, R., and Francia, G. D.: Calibrating chemical multisensory devices for real world applications: An in-depth comparison of quantitative machine learning approaches, *Sensors Actuators B, Chem.*, 255, 1191-1210, <https://doi.org/10.1016/j.snb.2017.07.155>, 2018.

595 Wang, Y. H., Hu, B., and Wang, Y. S.: Ozone weekend effects in the Beijing–Tianjin–Hebei metropolitan area, China, *Atmos. Chem. Phys. Discuss.*, 13, 13045–13078, <https://doi.org/10.5194/acp-14-2419-2014>, 2013.

600 Wei, P., Ning, Z., Ye, S., Sun, L., Yang, F., Wong, K. C., Westerdahl, D., Louie, P.: Impact analysis of temperature and humidity conditions on electrochemical sensor response in ambient air quality monitoring, *Sensors (Basel, Switzerland)*, 18(2), 59, <https://doi.org/10.3390/s18020059>, 2018.

605 Weissert, L., Alberti, K., Miles, E., Miskell, G., Feenstra, B., Henshaw, G. S., Papapostolou, V., Patel, H., Polidori, A., Salmond, J. A., and Williams, D. E.: Low-cost sensor networks and land-use regression: Interpolating nitrogen dioxide concentration at high temporal and spatial resolution in Southern California, *Atmos. Environ.*, 223, 117287, <https://doi.org/10.1016/j.atmosenv.2020.117287>, 2020.

610 World Health Organization, 2016. WHO Global Urban Ambient Air Pollution Database. Available at: https://www.who.int/phe/health_topics/outdoorair/databases/cities/en/, Accessed date: May 4, 2020.

615 World Health Organization, May 2, 2018. 9 out of 10 People Worldwide Breathe Polluted Air, but More Countries Are

Taking Action. Available at.

580 <https://www.who.int/news/item/02-05-2018-9-out-of-10-people-worldwide-breathe-polluted-air-but-more-countries-are-taking-action>, Accessed date: 16 September 2018.

Wu, Y., Zhang, S., Hao, J. M., Liu, H., Wu, X., Hu, J. N., Walsh, M. P., Wallington, T. J., Zhang, K. M., and Stevanovic, S.: On-road vehicle emissions and their control in China: a review and outlook, *Sci. Total Environ.*, 574, 332-349, <https://doi.org/10.1016/j.scitotenv.2016.09.040>, 2017.

585 Xie, M., Zhu, K., Wang, T., Chen, P., Han, Y., Li, S., Zhuang, B. L., and Shu, L.: Temporal characterization and regional contribution to O₃ and NOx at an urban and a suburban site in Nanjing, China. *Sci. Total Environ.*, 551-552, 533-545, <https://doi.org/10.1016/j.scitotenv.2016.02.047>, 2016.

Xie, Y., Zhao, B., Zhang, L., and Luo, R.: Spatiotemporal variations of PM_{2.5} and PM₁₀ concentrations between 31 Chinese cities and their relationships with SO₂, NO₂, CO and O₃, *Particuology*, 20, 141-149, <https://doi.org/10.1016/j.partic.2015.01.003>, 2015.

590 Xu, H., Bechle, M. J., Wang, M., Szpiro, A. A., Vedral, S., Bai, Y. Q., and Marshall, J. D.: National PM_{2.5} and NO₂ exposure models for China based on land use regression, satellite measurements, and universal kriging, *Sci. Total Environ.*, 655, 423-433, <https://doi.org/10.1016/j.scitotenv.2018.11.125>, 2019.

Xu, Z., Huang, X., Nie, W., Chi, X., Xu, Z., Zheng, L., Sun, P., and Ding, A. J.: Influence of synoptic condition and holiday effects on VOCs and ozone production in the Yangtze River Delta region, China, *Atmos. Environ.*, 168, 112-124, <https://doi.org/10.1016/j.atmosenv.2017.08.035>, 2017.

Yang, S., Wu, J., Du, Y., He, Y., and Chen, X.: Ensemble learning for short-term traffic prediction based on gradient boosting machine, *Journal of Sensors*, 2017, 1-15, <https://doi.org/10.1155/2017/7074143>, 2017.

600 Zhang, H., Xu, T., Zong, Y., Tang, H., Liu, X., and Wang, Y. C.: Influence of meteorological conditions on pollutant dispersion in street canyon, *Procedia Engineering*, 121, 899-905, <https://doi.org/10.1016/j.proeng.2015.09.047>, 2015.

Zhang, R., Zhang, Y., Lin, H., Feng, X., Fu, T. M., and Wang, Y. H.: NOx emission reduction and recovery during COVID-19 in east China, *Atmosphere*, 11, 433, <http://doi.org/10.3390/atmos11040433>, 2020.

605 Zhang, Y. X., Ye, X. P., Wang, S. B., He, X. J., Dong, L. Y., Zhang, N., Wang, H. K., Wang, Z. R., Ma, Y., Wang, L., Chi, X. G., Ding, A. J., Yao, M. Z., Li, Y. P., Li, Q. L., Zhang, L., and Xiao, Y. L.: Large-eddy simulation of traffic-related air pollution at a very high-resolution in a mega-city: Evaluation against mobile sensors and insights for influencing factors, <https://doi.org/10.5194/acp-2020-1168>, 2020.

Zhao, Y., Qiu, L. P., Xu, R. Y., Xie, F. J., Zhang, Q., Yu, Y. Y., Nielsen, C. P., Qin, H. X., Wang, H. K., Wu, X. C., Li, W. Q., and Zhang, J.: Advantages of a city-scale emission inventory for urban air quality research and policy: The case of Nanjing, a typical industrial city in the Yangtze River Delta, China, *Atmos. Chem. Phys.*, 15, 12623-12644, <http://doi.org/10.5194/acp-15-12623-2015>, 2015.

Zheng, B., Huo, H., Zhang, Q., Yao, Z. L., Wang, X. T., Yang, X. F., Liu, H., and He, K. B.: High-resolution mapping of vehicle emissions in China in 2008, *Atmos. Chem. Phys.*, 14, 9787-9805, <https://doi.org/10.5194/acp-14-9787-2014>, 2014.

615 Zhu, Y. F., Pudota, J., Collins, D., Allen, D., Clements, A., DenBleyker, A., Fraser, M., Jia, Y. L., McDonald-Buller, E., and Michel, E.: Air pollutant concentrations near three Texas roadways, Part I: Ultrafine particles, *Atmos. Environ.*, 43(30), 4513-4522, <https://doi.org/10.1016/j.atmosenv.2009.04.018>, 2009.

Zou, C., Wu, L., Li, X., Yuan, Y., Jing, B., and Mao, H. J.: Relationship between traffic flow and temporal and spatial variations of NO₂ and CO in Nanjing, *Acta Sci. Circumstantiae.*, 37(10), 3894-3905, <https://doi.org/10.13671/j.hjkxxb.2017.0374>, 2017.

SUPPLEMENTARY INFORMATION FOR Mobile monitoring of urban air quality at high spatial resolution by low-cost sensors: Impacts of COVID-19 pandemic lockdown

625 Shibao Wang¹, Yun Ma¹, Zhongrui Wang¹, Lei Wang¹, Xuguang Chi¹, Aijun Ding¹, Mingzhi Yao²,
Yunpeng Li², Qilin Li², Mengxian Wu³, Ling Zhang³, Yongle Xiao³, Yanxu Zhang¹

¹School of Atmospheric Sciences, Nanjing University, Nanjing, China

²Beijing SPC Environment Protection Tech Company Ltd., Beijing, China

³Hebei Saihero Environmental Protection Hi-tech. Company Ltd., Shijiazhuang, China

630 Correspondence to: Yanxu Zhang (zhangyx@nju.edu.cn)

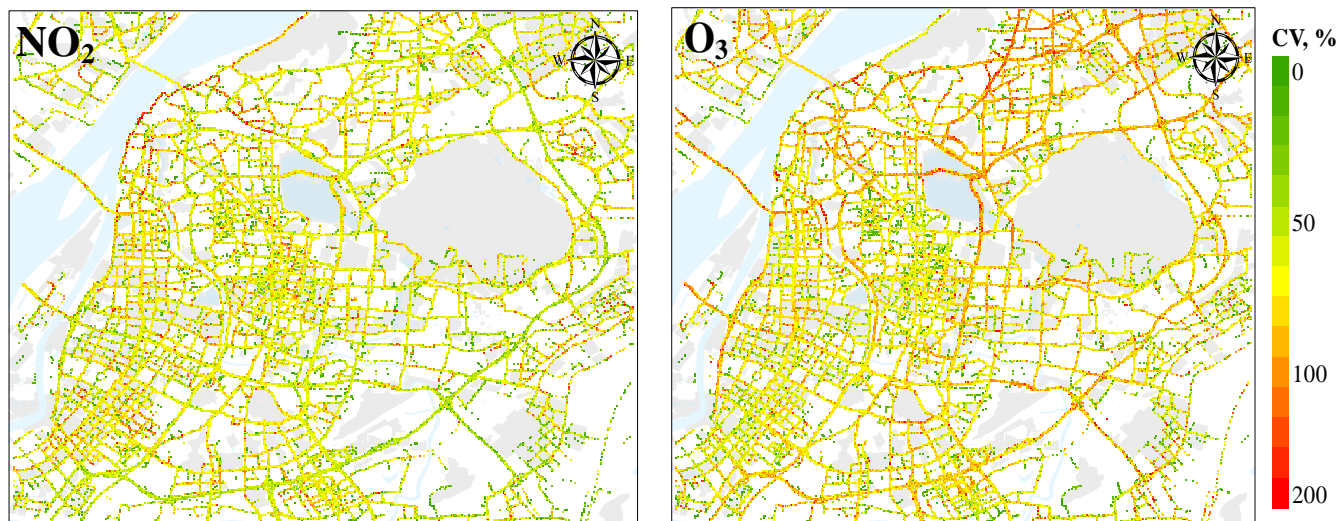


Figure S1. Spatial distribution of coefficient of variation for NO_2 and O_3 in 50 m grids in research domain. © OpenStreetMap contributors 2019. Distributed under a Creative Commons BY-SA License.

635

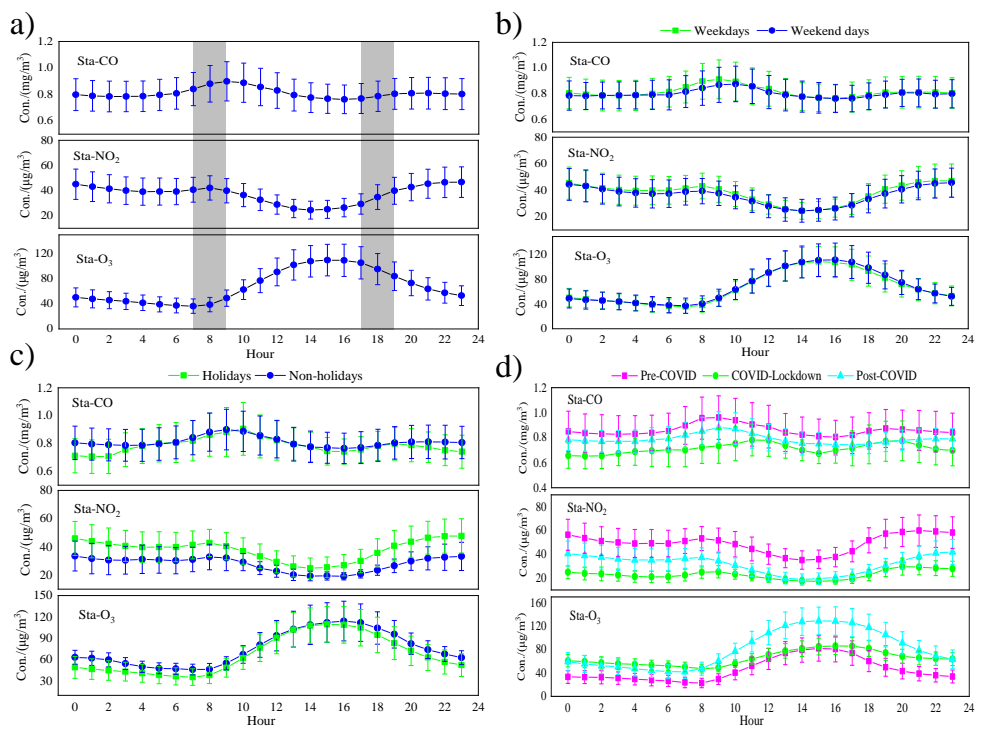


Figure S2. Diurnal cycles of three pollutant concentrations measured in rush/non-rush hours, weekdays/weekend days, holidays/non-holidays, and different stage of the COVID-19 pandemic by the stations sites data. Error bars show the standard deviation of observations. Gray areas represent the rush hours, and the other represents the non-rush hours.

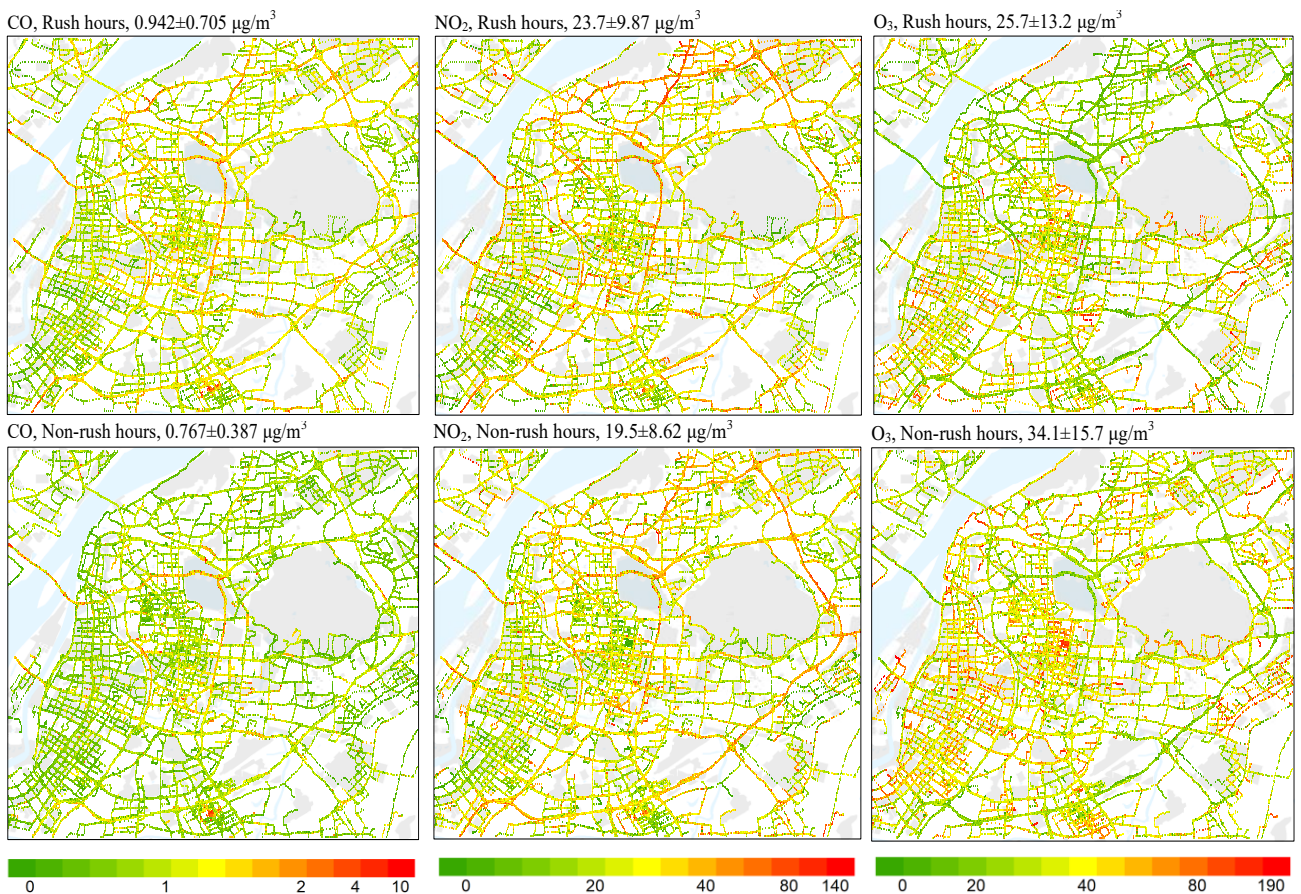


Figure S3. Spatial variation of CO, NO₂, and O₃ concentrations in rush hours and non-rush hours in the research area. © OpenStreetMap contributors 2019. Distributed under a Creative Commons BY-SA License.

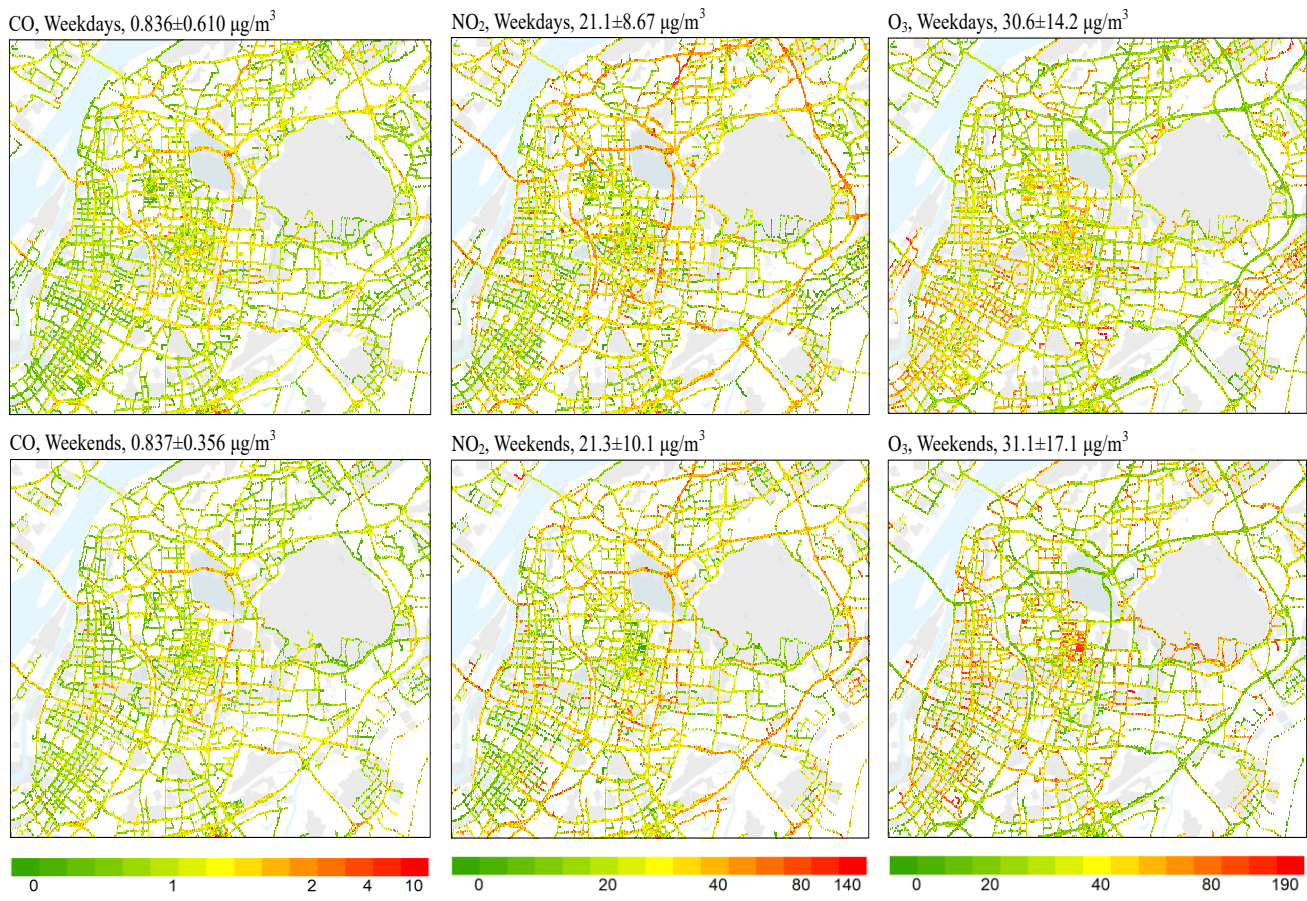


Figure S4. Spatial variation of CO, NO₂, and O₃ concentrations in weekdays and weekend days in the research area. © OpenStreetMap contributors 2019. Distributed under a Creative Commons BY-SA License.

645



Figure S5. Spatial variation of CO, NO₂, and O₃ concentrations in holiday and non-holiday in the research area. © OpenStreetMap contributors 2019. Distributed under a Creative Commons BY-SA License.

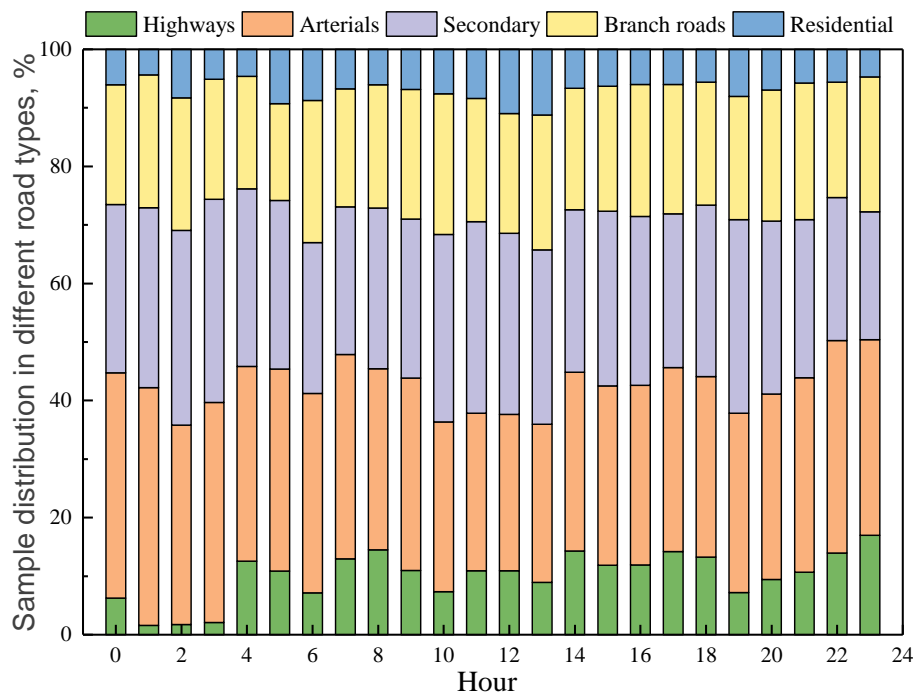
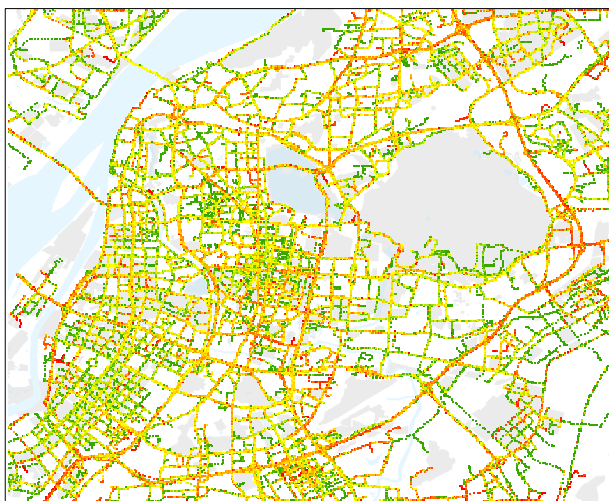


Figure S6. Hourly variation of mean sampling number in different types of roads during the whole sampling campaign.

650 c), NO₂, BS method, %



d), NO₂, PD method, %

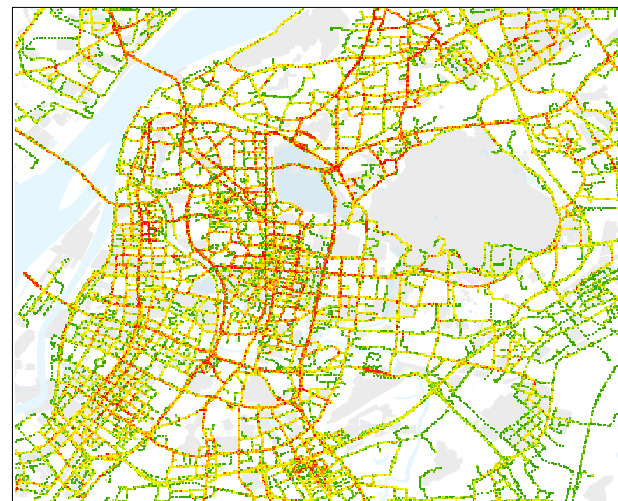
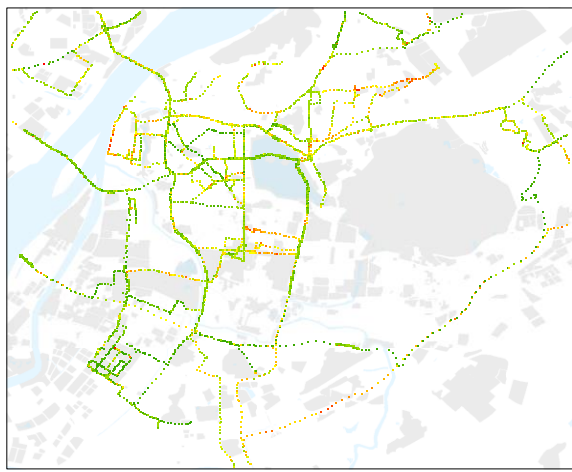
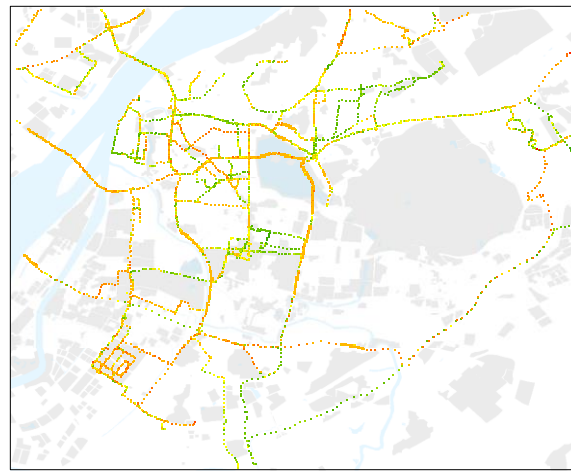


Figure S7. Contributions from traffic-related emissions calculated by stationary data method (c) and peak detection algorithm (d) for NO₂. © OpenStreetMap contributors 2019. Distributed under a Creative Commons BY-SA License.

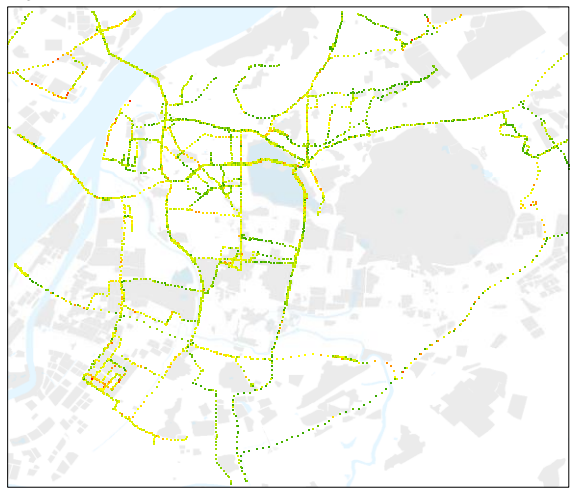
NO₂, P1→P2, Concentration variation: -41.7 %



NO₂, P2→P3, Concentration variation: +48.2 %



O₃, P1→P2, Concentration variation: +35.7 %



O₃, P2→P3, Concentration variation: +48.7 %

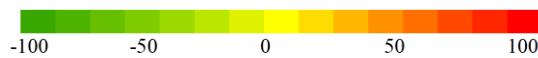
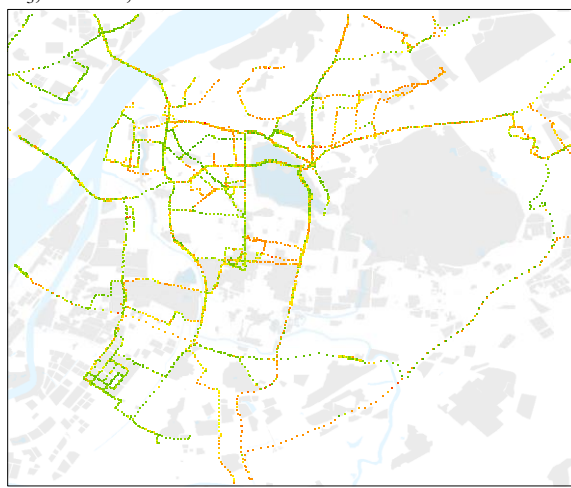
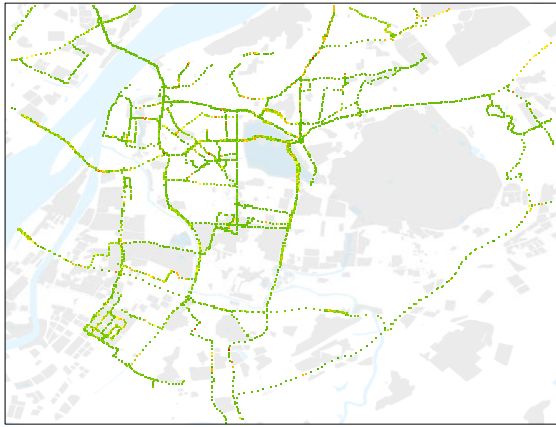


Figure S8. Changes of observed NO₂ and O₃ concentrations in the three stages of the COVID-19 pandemic. P1, P2, and P3 are for pre-COVID, COVID-Lockdown, and post-COVID periods, respectively. © OpenStreetMap contributors 2019. Distributed under a Creative Commons BY-SA License.

NO₂, P1→P2, Traffic emission: -51.8 %

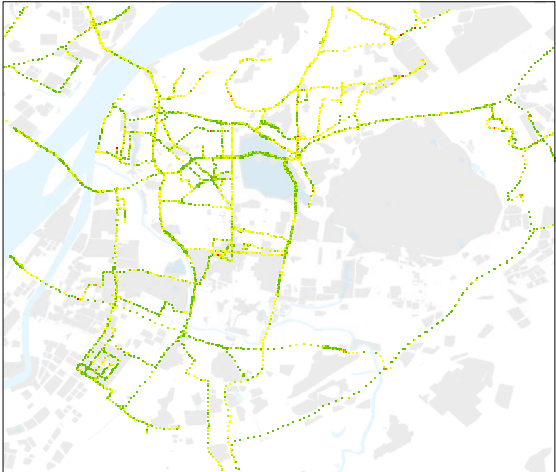


NO₂, P2→P3, Traffic emission: +131 %

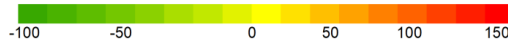
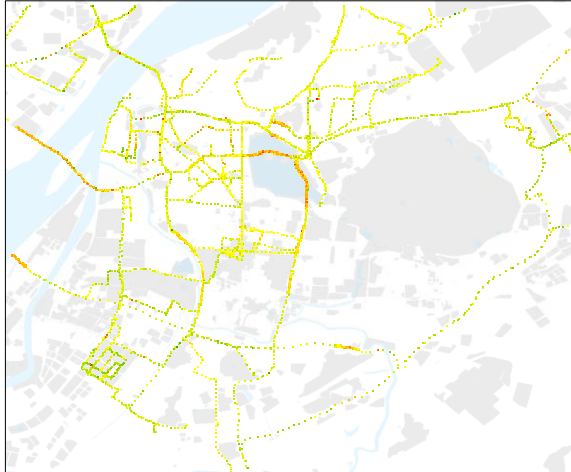


660

O₃, P1→P2, Traffic emission: -32.5 %



O₃, P2→P3, Traffic emission: +39.3 %



665

Figure S9. Changes of the contributions of traffic-related sources to NO₂ and O₃ in the three stages of the COVID-19 pandemic calculated by BS method. P1, P2, and P3 are for pre-COVID, COVID-Lockdown, and post-COVID periods, respectively. © OpenStreetMap contributors 2019. Distributed under a Creative Commons BY-SA License.